Reducing affinity as a strategy to boost immunomodulatory antibody agonism

Xiaojie Yu[1], Christian M Orr[2], H.T. Claude Chan[1], Sonya James, Christine A. Penfold[1], Jinny Kim[1], Tatyana Inzhelevskaya[1], C. Ian Mockridge[1], Kerry L Cox[1], Jonathan W. Essex[3, 4], Ivo Tews[3,5], Martin J. Glennie[1] and Mark S. Cragg[1,3,*]

[1]Antibody and Vaccine Group, Centre for Cancer Immunology, School of Cancer Sciences, University of Southampton Faculty of Medicine, Southampton, SO16 6YD, UK; [2]Diamond Light Source, Harwell Science and Innovation Campus, Didcot, OX11 0GD, UK; [3]Institute for Life Sciences, University of Southampton, Southampton SO17 1BJ, UK; [4]University of Southampton, School of Chemistry; Southampton SO17 1BJ, UK; [5]University of Southampton, Biological Sciences; Southampton SO17 1BJ, UK.

Corresponding author msc@soton.ac.uk

Keywords: immunostimulatory, antibodies, agonism, affinity, CD40, 4-1BB, PD-1, immunotherapy

Antibody responses during infection and vaccination typically undergo affinity maturation to achieve high affinity binding for efficient pathogen neutralization[1,2]. Similarly, high affinity is routinely the goal for therapeutic antibody generation. However, in contrast to naturally-occurring or direct-targeting therapeutic antibodies, immunomodulatory antibodies - designed to modulate receptor signalling, have not been widely examined for their affinity-function relationship. Here, examining three separate immunologically important receptors (CD40, 4-1BB and PD-1), spanning two receptor super-families, we show low, rather than high affinity delivers greater activity through increased clustering. This approach delivered higher immune cell activation, in vivo T cell expansion and anti-tumor activity in the case of CD40 and transformed an inert anti-4-1BB mAb into an agonist. Low affinity variants of the clinically important antagonistic anti-PD-1 mAb nivolumab also mediated more potent signalling, with impacts on T cell activation. These findings reveal a new paradigm for augmenting agonism across diverse receptor families and shed light on the mechanism of antibody-mediated receptor signalling. Such affinity engineering offers a rational, efficient and highly tunable solution to deliver antibody-mediated receptor activity across a range of potencies suitable for translation to the treatment of human disease.

Main text

The humoral immune response constitutes a major component of immunity. Antibody responses during infection and vaccination typically undergo affinity maturation, leading to the selection of B cell clones that produce higher affinity antibodies[2]. Such antibodies are required for efficient pathogen opsonisation and can be sufficient for pathogen neutralization[3]. This high affinity and specificity for target antigen has seen antibodies broadly adopted as the biologic of choice in the treatment of many diseases, with over 100 monoclonal antibodies (mAb), now approved for use in humans[4,5]. Current approaches for generating therapeutic mAb, including hybridoma technology[6], antibody display platforms[7] and direct sequencing modalities[8], have typically prioritised high affinity as a key criteria for selection. High affinity is critical for the activity of naturally-occurring and conventional direct-targeting therapeutic antibodies which bind to antigens on pathogens or tumor cells and commonly require Fc-mediated immune effector functions for full therapeutic activity. A conceptually distinct

class of mAb are agonistic and target immune receptors such as TNF receptors (TNFR) CD40 and 4-1BB to induce intracellular signalling[9]. Compared with direct-targeting mAb, the rules governing the activity of agonistic mAb are more complex and multifactorial, determined by a combination of antibody epitope, isotype and Fc gamma receptor (FcγR) requirements[10-12]. These agonistic mAb have entered clinical trials and offer promise for cancer immunotherapy[9]. However, unlike conventional direct-targeting mAb no study has systematically examined the impact of affinity on their activity, and it remains unclear whether high affinity is similarly important.

Generation of anti-CD40 affinity variants

To investigate the effect of affinity on the agonistic activity of immunostimulatory receptor mAb, we chose the human CD40 system as a paradigm and used a crystal structure of CD40 in complex with the F(ab) of a clinically-relevant anti-CD40 mAb ChiLob 7/4 as a model to design affinity mutants based on the complementary determining regions (CDR). The crystal structure was analysed in PISA using the QtPISA interface to identify potential interacting residues which were then mutated to alanine in PyMol and subsequently re-analysed in PISA. The resulting difference in deltaG and binding energy were used to predict the effect of mutations on binding affinity. A series of single, double and triple mutants were subsequently evaluated with the application of a confusion matrix to produce combined mutation scores, and final mutations were determined based on the scores in the confusion matrix and the proximity of the residue to the binding interface. In addition, we took advantage of a series of non-CDR, framework mutants generated during the humanization of ChiLob 7/4. Thus, we produced 6 mutants by mutating the CDR sequence (prefixed CDR-), and 6 mutants by altering the variable domain framework sequence (prefixed FW-) (Fig. 1a). Surface plasmon resonance (SPR) revealed these ChiLob 7/4 mutants bound CD40 with a range of affinities (5.22 – 925 nM) differing in both the on- and off-rates (Fig. 1b, Extended Data Fig. 1a, b). We previously demonstrated that antibody epitope could significantly influence the agonistic activity of anti-CD40 mAb[11]; therefore, we performed competitive cell binding assays which showed that they could differentially inhibit WT ChiLob 7/4 binding to CD40 in a dose-dependent manner according to their respective CD40 binding affinities, supporting that they bound cell surface CD40 via the same epitope (Extended Data Fig. 1c).

Low affinity anti-CD40 mAb show greater agonism

We next examined the activity of these mAb in the human CD40 transgenic (hCD40 Tg) mouse system[13]. As most anti-CD40 mAb require FcγR2b cross-linking for agonistic activity[10,14], we initially expressed the ChiLob 7/4 mutants as mIgG1 to enable efficient engagement with mouse FcγR2b[10]. Splenic B cells from hCD40Tg mice were treated with these anti-CD40 affinity variants and then levels of activatory markers, CD23 and CD86, and B cell proliferation assessed. Contrary to expectations from direct targeting mAb, anti-CD40 antibodies with lower affinity exhibited stronger agonistic activity evidenced by upregulation of CD23 and CD86, and increased B cell proliferation and cell:cell homotypic adhesion (Fig. 1c-e, Extended Data Fig. 2a-c). The affinity-agonism relationship revealed a bell-shaped curve whereby B cell activation increased from the parental ChiLob 7/4 mIgG1 baseline with reducing affinity until a threshold was reached where proliferation fell (Fig. 1c-e). The most agonistic variants (FW-16 mIgG1 and CDR-Y102A/Y32A mIgG1) induced approximately 26-fold and 8-fold higher CD23 and CD86 expression, respectively (Fig. 1c, d) than the WT mAb. The same bell-shaped response between agonism and affinity was seen in B cell proliferation where the most agonistic variant induced 2-fold higher proliferation (Fig. 1e). Although the magnitude of the effect differs between these readouts, indicating a differential threshold for activation (with CD23 expression the lowest and proliferation the highest), they all confirm that lower affinity drives increased agonism. Moreover, in each case mAb off-rate (kd), but not on-rate (ka), exhibited a similar bell-shaped trend as the equilibrium affinity (KD; Extended Data Fig. 2a-c), indicating it was the driving parameter.

To investigate whether such low affinity-driven agonism could be recapitulated in vivo, we used an OTI CD8 T cell expansion model in which mice were injected with ovalbumin (OVA)-specific OTI cells followed by the administration of OVA and low affinity anti-CD40 variants[12]. Consistent with the in vitro data, the low affinity mAb induced significantly higher levels of antigen-specific CD8 T cell expansion, identified by SIINFEKL tetramer staining, with the most agonistic variant FW-16 mIgG1 inducing 8-fold higher expansion than the WT parental mAb (Fig. 2a, b). Interestingly CDR-Y102A/Y32A mIgG1 which displayed equally strong agonistic activity as FW-16 mIgG1 in vitro mediated a more modest enhancement in OTI expansion, indicating that the precise affinity range for

maximal agonism differed among the experimental systems. We next examined whether enhanced agonism could be translated into therapeutic benefit in the OVA+ EG7 tumor model. Mice were inoculated with EG7 tumor subcutaneously and then treated with anti-CD40 mAb when tumors became palpable. The ability of low-affinity anti-CD40 mAb to drive robust tumor-specific T cell responses was retained in tumor-bearing mice (Fig. 2c). Moreover, while the parental mAb conferred a modest degree of survival benefit compared with the isotype control, the low affinity variant CDR-Y102A/Y32A mIgG1 was able to cure the majority of mice and was significantly more effective than the higher affinity parent mAb (Fig. 2d, Extended Data Fig. 2d). In addition, cured mice were resistant to tumor rechallenge, demonstrating robust immunological memory (Fig. 2e). These data collectively demonstrate that low affinity anti-hCD40 mAb are able to mediate superior agonistic activity in vitro and in vivo and exhibit potent antitumor activity versus the high affinity parent antibody.

Strong agonistic activity in human systems

We next examined whether low affinity-mediated agonism could be recapitulated in human systems. As the mIgG1 isotype effectively engages with mouse but not human FcγRs, we isotype-switched the ChiLob 7/4 mIgG1 variants to the hIgG2 isotype, optimal for receptor agonism[11,12,15]. SPR analysis showed that these hIgG2 affinity variants exhibited an affinity ranking for CD40 similar to their mIgG1 counterparts (Extended Data Fig. 3a, b). Moreover, they dose-dependently inhibited the binding of WT ChiLob7/4 to Ramos cells, as anticipated from their affinities, again supporting a conserved epitope (Extended Data Fig. 3c). Consistent with previous data using mIgG1 mAb, the low affinity ChiLob 7/4 hIgG2 variants induced greater levels of CD23 and CD86 expression on hCD40Tg B cells as well as more proliferation compared with the WT ChiLob 7/4 hIgG2 mAb (Extended Data Fig. 3d, e), and more robust OTI expansion in vivo (Extended Data Fig. 3f). Purified human B cells also underwent more robust proliferation and displayed higher expression of CD23 and CD86 in response to low affinity ChiLob 7/4 hIgG2 variants (Extended Data Fig. 3g, h, i). Next, as CD40 stimulates immune responses primarily through DCs[16], we derived immature DCs from CD14+ human monocytes and found that low affinity ChiLob 7/4 hIgG2 variants induced higher levels of CD86 expression than parental (higher affinity) ChiLob 7/4 hIgG2, a well-established marker for DC activation (Extended Data Fig. 4a, b).

Moreover, in a mixed leukocyte reaction, DCs treated with low affinity variants induced more robust allogeneic T cell proliferation, demonstrating that these activated DCs were functional with enhanced ability to stimulate T cells (Extended Data Fig. 4c, d). Furthermore, in a human PBMC antigen recall assay where a mixture of viral and bacterial peptide antigens were used to elicit a T cell recall response, low affinity ChiLob 7/4 hIgG2 mAb induced higher levels of CD25 expression on the responding proliferating T cells (Extended Data Fig. 4e, f). These data collectively demonstrate that low affinity anti-CD40 hIgG2 mAb induced higher levels of agonism in human systems than parental higher affinity ChiLob 7/4 hIgG2.

Greater receptor clustering independent of FcγR drives agonism

After establishing that low affinity anti-CD40 mAb induced superior agonism than parental WT mAb, we investigated the underlying mechanism. The agonistic activity of anti-CD40 mAb is governed by a complex interplay between epitope and isotype, which mediates differential levels of receptor clustering[11,15,17]. We hypothesized that low affinity mAb that retained sufficient antigen binding induced higher agonism through increased receptor clustering, which was independent of FcγR engagement. We tested this latter hypothesis by employing Jurkat-NFκB-GFP reporter cells that express hCD40 but lack FcγR expression, utilising the mIgG1 isotype as it lacks intrinsic Fc-dependent, FcγR-independent agonistic activity[12] so that any increased agonism could be solely attributed to the affinity effect. Consistent with our hypothesis, low affinity ChiLob 7/4 mIgG1 variants induced significantly higher levels of NFκB activation compared with the higher affinity WT parent (Fig. 3a, Extended Data Fig. 5a). In confirmation, we used B cells purified from hCD40Tg/FcγRnull mice that lack all FcγR[15], and showed that low affinity variants induced significantly more CD23 and CD86 and higher levels of B cell proliferation and cell:cell homotypic adhesion (Fig. 3b-d, Extended Data Fig. 5b-d). Although the presence of the inhibitory FcγR2b produced greater agonism, with higher expression of CD23 and CD86 and more B cell proliferation in WT versus FcγRnull B cells, its enhancing effect was less apparent with low affinity variants, supporting that they induce agonism in a distinct manner, independently of FcγR interaction (Fig. 3e-h). Nonetheless, it is clear FcγR interaction can influence receptor agonism in vivo and differential FcγR expression in different disease contexts may modulate

activity. We also noted low affinity antibodies do not require saturating concentrations to sustain their agonistic activity, with reduced receptor engagement by low affinity variants driving more powerful agonism (Fig. 3i, j). Low affinity ChiLob 7/4 hIgG2 mutants also induced more robust CD23 and CD86 upregulation and B cell proliferation in hCD40Tg/FcγRnull B cells (Extended Data Fig. 6). These data demonstrated that low affinity mAb-mediated agonism of CD40 was independent of FcγRs.

To further unravel the molecular mechanism of low affinity-induced agonism, we evaluated the ability of ChiLob 7/4 variants to induce CD40 clustering. We previously demonstrated that TNFR agonists induce differential agonistic activity through distinct patterns of receptor clustering[17]. In order to better distinguish and quantify the level of receptor clustering among the low affinity antibody variants, we used Jurkat cells expressing GFP-CD40 (Jurkat-CD40-GFP) that lacked FcγRs, quantifying the level of receptor clustering by employing a clustering index (see methods), with higher numbers denoting greater receptor clustering (Extended Data Fig. 7a). Jurkat-CD40-GFP cells treated with low affinity ChiLob 7/4 mIgG1 variants induced significantly greater levels of receptor clustering with a higher clustering index than the WT mIgG1 parent that did not induce appreciable clustering (Fig. 3k, l, Extended Data Fig. 7b). This demonstrated that for antibodies sharing the same isotype and epitope, lowering the affinity evoked enhanced receptor clustering and downstream signalling. Augmented clustering was also supported qualitatively by z-stacked confocal images showing significant receptor redistribution and clustering for low affinity variants (Fig. 3m), which was not associated with changes in cell shape (Extended data Fig. 7c). Moreover, bivalent, but not monovalent Fab engagement, was required for agonism and receptor clustering (Extended Data Fig. 7d-f). In addition, low affinity mAb did not alter the extent of receptor internalization compared with higher affinity controls (Extended Data Fig. 7g, h). These data collectively demonstrated that low affinity anti-CD40 mAb mediated higher levels of agonistic activity through elevated receptor clustering, independent of FcγRs. To further dissect the subcluster structures underlying the differential agonism, we performed super-resolution dSTORM microscopy on Jurkat-CD40-GFP cells. Wide field fluorescence images showed that low affinity anti-CD40 mAb formed clusters predominantly at cell:cell junctions, unlike CD40 ligand (CD40L) which induced clusters more widely dispersed throughout the membrane (Extended Data Fig.

8a). However, at the subcluster level evaluated by dSTORM, differences were less obvious, with ChiLob 7/4 hIgG2, FW-16 mIgG1 and FW-32 mIgG1, but not CD40L, displaying significantly higher density subclusters at the cell:cell junctions compared to untreated samples (Extended Data Fig. 8b). Moreover, correlation analysis of area and density showed that CD40L induced fewer medium and large subclusters of medium-high density than ChiLob 7/4 hIgG2, FW-16 mIgG1 and FW-32 mIgG1 (Extended Data Fig. 8c). These results indicate that subclusters within mAb and ligand-induced clusters are similar in density but differ significantly in their membrane localization.

Low affinity anti-4-1BB mAb elicit agonism

We next explored whether the low affinity-mediated agonism observed with anti-CD40 mAb was applicable to other TNFR, and chose 4-1BB, another costimulatory TNFR of interest in cancer immunotherapy[18]. To date, two anti-4-1BB mAb have entered clinical trials with differing outcomes. While urelumab demonstrated strong pharmacodynamic effects accompanied by liver toxicity, utomilumab was quiescent on both fronts[18]. In agreement, we previously showed that urelumab evoked strong receptor clustering and activity in multiple isotypes, whereas utomilumab even as a hIgG2 did not elicit receptor clustering or activity[17]. Therefore, we chose to generate affinity variants for utomilumab in an attempt to elicit agonism for this otherwise inert mAb. Based on the crystal structure of the utomilumab F(ab):4-1BB complex[19], we generated a panel of affinity mutants by undertaking a similar approach to before (Fig. 1a), mutating the key residues within the CDRs (Fig. 4a). The mutants exhibited lower binding to 4-1BB immobilized on an SPR chip compared with the WT mAb (Fig. 4b, Extended Data Fig. 9a), and less binding to 4-1BB expressed at the cell surface (Fig. 4c). Moreover, the low affinity mutants mediated less potent macrophage-mediated ADCP and human PBMC-mediated ADCC (Fig. 4d,e), consistent with high affinity binding being required for efficient Fc-mediated antibody effector functions. In contrast to reduced Fc-mediated effector functions, the low affinity utomilumab variants induced significantly higher levels of NFκB activation in Jurkat-NFκB-GFP reporter cells expressing h4-1BB, while the WT utomilumab was inactive as expected (Fig. 4f). Enhanced NFκB activity correlated with more efficient receptor clustering, evidenced by a higher clustering index and visible clusters in confocal microscopy (Fig. 4g,h, Extended Data Fig. 9b). In

addition, the lower 4-1BB binding affinity correlated positively with a higher clustering index (Fig. 4i), but not with changes in cell shape (Extended data Fig. 9c). Similar to anti-CD40 mAb, low affinity anti-4-1BB mAb also required bivalent receptor engagement for agonistic activity and receptor clustering (Fig. 4j-l) but not saturating mAb concentrations for sustained agonistic activity (Fig. 4m,n). These data showed that as with anti-CD40 mAb, low affinity anti-4-1BB mAb mediate higher agonistic activity, suggesting that low affinity antibody-induced agonism is a conserved feature among TNFR.

Low affinity anti-PD-1 mAb elicit agonism

To explore whether this low affinity effect observed with mAb directed to TNFR was applicable to other receptors that mediate receptor signalling, we chose to evaluate the most clinically important immune checkpoint receptor, PD-1. Antagonistic anti-PD-1 mAb that block PD-1 signalling represent a major breakthrough in cancer immunotherapy and have been approved in multiple cancer types[20]. Recently, agonistic anti-PD-1 mAb, designed to induce active PD-1 signalling, have been suggested as potential therapeutics for autoimmune diseases such as systemic lupus erythematosus and psoriasis[21-23]. Based on the crystal structure of PD-1 in complex with the clinically approved antagonistic anti-PD-1 mAb nivolumab[24], we designed a panel of mutants as before to investigate the effect of mAb affinity on PD-1 agonism (Fig. 5a). SPR analysis showed the nivolumab mutants exhibited a range of affinities towards immobilized PD-1 (Extended Data Fig. 9f, g), spanning 28 fold difference from WT nivolumab and bound cell surface PD-1 accordingly (Extended Data Fig. 9h). To evaluate the ability of these mAb to block the PD-1:PD-L1 interaction, we developed an assay where PD-1-transfected Jurkat-NFAT-Luc cells, which exhibit luciferase activity upon NFAT activation, were mixed with CHO cells expressing PD-L1 and an anti-CD3-scFv designed to engage CD3 on the Jurkat cells to induce NFAT activation (Extended Data Fig. 10a, left panel). The mutants dose-dependently rescued NFAT activation from PD-L1-mediated suppression with the blocking activity positively correlated with PD-1 binding affinity (Fig. 5b), reducing as affinity decreased. These data demonstrate that blockade of PD-1:PD-L1 is dependent on high affinity anti-PD-1 mAb as expected. Next, to investigate the impact of affinity on cell-intrinsic PD-1 signalling we designed a chimeric PD-1 construct, replacing the intracellular signalling domain of PD-1 with that of CD40, and generated Jurkat-NFκB-GFP cells stably expressing

this construct to assess PD-1 signalling directly in response to anti-PD-1 treatment (Extended Data Fig. 10a, middle panel). As shown in Fig. 5c, the WT nivolumab and its high affinity variant T28A were unable to induce PD-1 signalling, whereas the low affinity variants induced significant signalling in a dose-dependent manner, similar to the anti-CD40 and anti-4-1BB affinity variants described earlier (Fig. 3a, Fig. 4f). As PD-1 is known to signal concurrently with the TCR complex to deliver negative signals in T cells[22,25-27], we next examined whether PD-1 signalling induced by low affinity variants would impair CD3-mediated T cell activation. To this end we generated CHO cells expressing a scFv specific for hIgG Fc to capture both anti-CD3 and anti-PD-1 mAb and then incubated these mAb-coated CHO cells with PD-1-transfected Jurkat-NFAT-Luc cells; thereafter measuring NFAT signalling and CD69 expression to assess T cell activation (Extended Data Fig. 10a, right panel). As expected, the CHO cells captured the anti-PD-1 variants equivalently (Extended Data Fig. 10b); moreover, the WT anti-PD-1 mAb suppressed anti-CD3-induced T cell activation as evidenced by reduced NFAT signalling and CD69 downregulation compared with the isotype control (Fig. 5d, e). Low affinity nivolumab variants exhibited stronger T cell suppression than the WT parent, with affinity correlated to reduced NFAT signalling and CD69 expression (Fig. 5d, e). Notably, lower affinity variants induced equal levels of suppression to soluble PD-L1. Moreover, mAb off-rate, but not on-rate, displayed inverse correlation with NFAT signalling and CD69 expression (Extended Data Fig. 10c, d). These data demonstrate low affinity anti-PD-1 variants induced stronger PD-1 signalling and T cell suppression.

To uncover the molecular mechanism, we investigated the ability of the same variants to induce PD-1 clustering using IIA1.6 cells stably transfected with GFP-PD-1 and lacking FcγRs[28]. Untreated cells, cells treated with parental nivolumab or higher affinity variants did not display significant PD-1 clustering. In contrast, almost all low affinity variants induced significant PD-1 clustering coincident with increased clustering index (Fig. 5f, Extended Data Fig. 10e), corroborated by confocal microscopy (Fig. 5g, Extended Data Fig. 10f). Similar to the CD40 system, low affinity anti-PD-1 mAb did not induce significant receptor internalization (Fig. 5h, i) and saturating mAb concentrations were not required for sustained agonism (Extended Data Fig. 10g). In addition, changes in cell shape did not correlate with agonism (Extended Data Fig. 10h). These data directly support that stronger mAb-

mediated agonism can be achieved by reducing affinity also for immune receptors outside of the TNFR family with a similar underpinning mechanism, independent of FcγR, changes to receptor internalization, or requiring saturating concentrations.

Discussion

Unlike natural and direct-targeting antibodies, agonistic immunomodulatory mAb differ in their mechanism of action, needing to elicit productive receptor signalling in addition to specific target engagement. Antibodies targeting TNFR remain highly studied due to their potential in cancer immunotherapy with epitope, isotype and FcγR engagement known to modulate activity[10-12].

Here, we investigated the impact of affinity on immunomodulatory mAb directed to 3 different receptors. In general, therapeutic antibodies are considered high affinity at KD <1 nM[29,30]. As epitope and isotype can impact mAb agonism as outlined above, we designed experiments where these aspects were controlled. Our structure-guided mutational approach did not obviously alter specificity as affinity mutants retained binding for their target without exhibiting binding to close homologues (Extended Data Fig. 11a-f). Low affinity anti-CD40 mAb displayed augmented agonism compared with higher affinity parent molecules. The relationship between affinity and agonism was bell-shaped with activity increasing as affinity decreased until a threshold where activity dropped significantly, presumably due to insufficient target engagement. For ChiLob 7/4 this occurred at >288 nM, associated with an inability to compete with parental mAb for cell surface binding. Therefore, the application of low affinity agonism through rationale design is limited by the need to engage the receptor sufficiently on the target cell. Moreover, mAb off-rate, but not on-rate, exhibited a similar bell-shaped relationship with agonism in both FcγR-competent and FcγR-deficient systems, suggesting faster dissociation is responsible for increased agonistic activity of low affinity variants. In support, and in the reverse approach to ours, anti-Fas mAb engineered with higher-affinity demonstrated reduced activity, with lower off-rate the key determinant. It was proposed that mAb with slow dissociation rates “lock” two receptor monomers into a non-signaling complex, preventing receptor oligomerisation and activation[31]. These data support the hypothesis that high affinity binding is not essential for receptor agonism and moreover is detrimental.

289 Low affinity anti-CD40 mAb induced agonistic activity and significant receptor clustering independent
290 of FcγR, which supports the "fast dissociation" model and indicates agonism is mediated through
291 receptor clustering akin to conventional high affinity mAb[17]. Low affinity variants displayed enhanced
292 agonism also as hIgG2 mAb in various human assays, indicating that low affinity drives agonism
293 independently of isotype. Further studies are needed to evaluate the in vivo effect of the hIgG2 mAb in
294 a fully hFcγR-transgenic animal model. To extend the observation beyond CD40, we investigated the
295 anti-4-1BB mAb utomilumab which lacks intrinsic agonism[17,32]. Lowering utomilumab affinity led to
296 robust 4-1BB-mediated NFκB activation and enhanced receptor clustering. As with anti-CD40 mutants,
297 bivalency was required for low affinity agonism, with Fab fragments inactive. In contrast, lower affinity
298 provided reduced ADCC and ADCP. This divergent activity profile supports the paradigm that low
299 affinity targeting is conducive to receptor signaling but detrimental for Fc-mediated effector functions.
300 To assess whether low affinity targeting could be a general strategy to enhance receptor signaling
301 beyond TNFR, we generated affinity mutants of the anti-PD-1 mAb nivolumab[20]. Consistent with our
302 earlier findings, low affinity anti-PD-1 mAb induced greater PD-1 signaling through enhanced receptor
303 clustering, evoking more potent TCR-activated T cell suppression.

304 One possible mechanism underpinning low affinity mAb activity was reduced internalization evoked
305 by higher affinity mAb[33], resulting in elevated signaling through prolonged retention at the cell surface.
306 However, for all receptors examined this was not the case. In contrast, by confocal, but not quenching
307 assay, certain low affinity mAb appeared to display some vesicular internalization which may impact
308 their activity (Extended Data Fig. 11g-i). Low affinity agonism did not require constant receptor
309 saturation. Nevertheless, it remains possible that weaker interactions conferred by lower affinity mAb
310 may trigger sufficient agonism to drive activity but not negative feedback mechanisms as a rheostat,
311 thereby triggering higher net activity. Although unlikely, it is also possible that the introduced mutations
312 could evoke a small shift in the epitope bound by the affinity modified mAb, to enhance agonism.

313 Similar to ChiLob 7/4 mutants, the anti-PD-1 mAb off-rate correlated with T cell suppression. It is
314 therefore conceivable that all low affinity mutants employ a similar mechanism that requires partial
315 dissociation (afforded by high off-rate) to induce agonism, which is supported by their ability to mediate

receptor clustering and agonism independent of FcγRs. CDR-Y102A/Y32A m1, CDR-Y102A/Y50A and CDR-Y102A/Y32A/Y96A exhibited higher on-rate than the WT parent. Here, the Fab arms may engage the antigen sequentially, with less steric hindrance compared with higher affinity mAb which might be expected to engage the antigen with both Fab arms concurrently, with sequential engagement providing these mAb faster on-rates. Importantly, low affinity mutants induced stronger agonism at various receptor densities, encompassing physiological levels (Extended Data Fig. 11j-o). We also compared receptor clusters induced by low affinity mAb and natural ligands. dSTORM revealed that while low affinity anti-CD40 mAb-induced clusters were predominantly located at cell:cell junctions, ligand-induced clusters were dispersed throughout the cell membrane, consistent with our previous findings[17]; however, the subcluster density showed only modest differences between mAb and ligand, suggesting differential receptor cluster localization could influence agonistic activity. Conventional mAb and native TNFR ligands differ in their binding valency[34], reflected in their distinct binding kinetics to their cognate receptors (Extended Data Fig. 11p). Whether such differences in valency influences receptor cluster localization requires further investigation. It is also possible that these properties of the native ligand have evolved to elicit optimal, smaller, receptor clustering arrangements, not fully resolved by dSTORM, to deliver maximal receptor activity without the need for the larger clusters required by low affinity mAb.

In summary, our affinity approach provides an efficient alternative to generating large sets of novel mAb to achieve a desired receptor outcome. For three different receptors expressed on antigen presenting cells or T cells, spanning positive (immunostimulatory) and negative (checkpoint inhibitors) immune regulators we demonstrate that low affinity mAb deliver agonistic signaling. Such affinity engineering offers a broadly applicable, tractable, rational and highly tunable solution to deliver desired antibody-mediated receptor activity whereby a range of affinities mediate diverse activities suitable for translation in the human disease setting.

References

1 Muramatsu, M. *et al.* Class switch recombination and hypermutation require activation-induced cytidine deaminase (AID), a potential RNA editing enzyme. *Cell* **102**, 553-563 (2000). https://doi.org:10.1016/s0092-8674(00)00078-7

2 Viant, C. *et al.* Antibody Affinity Shapes the Choice between Memory and Germinal Center B Cell Fates. *Cell* **183**, 1298-1311 e1211 (2020). https://doi.org:10.1016/j.cell.2020.09.063

3 Forthal, D. N. Functions of Antibodies. *Microbiol Spectr* **2**, AID-0019-2014 (2014). https://doi.org:10.1128/microbiolspec.AID-0019-2014

4 Singh, S. *et al.* Monoclonal Antibodies: A Review. *Curr Clin Pharmacol* **13**, 85-99 (2018). https://doi.org:10.2174/1574884712666170809124728

5 Mullard, A. FDA approves 100th monoclonal antibody product. *Nat Rev Drug Discov* **20**, 491-495 (2021). https://doi.org:10.1038/d41573-021-00079-7

6 Kohler, G. & Milstein, C. Continuous cultures of fused cells secreting antibody of predefined specificity. *Nature* **256**, 495-497 (1975). https://doi.org:10.1038/256495a0

7 Clackson, T., Hoogenboom, H. R., Griffiths, A. D. & Winter, G. Making antibody fragments using phage display libraries. *Nature* **352**, 624-628 (1991). https://doi.org:10.1038/352624a0

8 Pedrioli, A. & Oxenius, A. Single B cell technologies for monoclonal antibody discovery. *Trends Immunol* **42**, 1143-1158 (2021). https://doi.org:10.1016/j.it.2021.10.008

9 Mayes, P. A., Hance, K. W. & Hoos, A. The promise and challenges of immune agonist antibody development in cancer. *Nat Rev Drug Discov* **17**, 509-527 (2018). https://doi.org:10.1038/nrd.2018.75

10 White, A. L. *et al.* Interaction with FcgammaRIIB is critical for the agonistic activity of anti-CD40 monoclonal antibody. *J Immunol* **187**, 1754-1763 (2011). https://doi.org:10.4049/jimmunol.1101135

11 Yu, X. *et al.* Complex Interplay between Epitope Specificity and Isotype Dictates the Biological Activity of Anti-human CD40 Antibodies. *Cancer cell* **33**, 664-675 e664 (2018). https://doi.org:10.1016/j.ccell.2018.02.009

12 White, A. L. *et al.* Conformation of the human immunoglobulin G2 hinge imparts superagonistic properties to immunostimulatory anticancer antibodies. *Cancer cell* **27**, 138-148 (2015). https://doi.org:10.1016/j.ccell.2014.11.001

13 Ahonen, C. *et al.* The CD40-TRAF6 axis controls affinity maturation and the generation of long-lived plasma cells. *Nat Immunol* **3**, 451-456 (2002). https://doi.org:10.1038/ni792

14 Dahan, R. *et al.* Therapeutic Activity of Agonistic, Human Anti-CD40 Monoclonal Antibodies Requires Selective FcgammaR Engagement. *Cancer cell* **29**, 820-831 (2016). https://doi.org:10.1016/j.ccell.2016.05.001

15 Yu, X. *et al.* Isotype Switching Converts Anti-CD40 Antagonism to Agonism to Elicit Potent Antitumor Activity. *Cancer cell* **37**, 850-866 e857 (2020). https://doi.org:10.1016/j.ccell.2020.04.013

16 Ma, D. Y. & Clark, E. A. The role of CD40 and CD154/CD40L in dendritic cells. *Semin Immunol* **21**, 265-272 (2009). https://doi.org:10.1016/j.smim.2009.05.010

17 Yu, X. *et al.* TNF receptor agonists induce distinct receptor clusters to mediate differential agonistic activity. *Commun Biol* **4**, 772 (2021). https://doi.org:10.1038/s42003-021-02309-5

18 Chester, C., Sanmamed, M. F., Wang, J. & Melero, I. Immunotherapy targeting 4-1BB: mechanistic rationale, clinical results, and future strategies. *Blood* **131**, 49-57 (2018). https://doi.org:10.1182/blood-2017-06-741041

19 Chin, S. M. *et al.* Structure of the 4-1BB/4-1BBL complex and distinct binding and functional properties of utomilumab and urelumab. *Nature communications* **9**, 4679 (2018). https://doi.org:10.1038/s41467-018-07136-7

20 Gong, J., Chehrazi-Raffle, A., Reddi, S. & Salgia, R. Development of PD-1 and PD-L1 inhibitors as a form of cancer immunotherapy: a comprehensive review of registration trials and future

considerations. *J Immunother Cancer* **6**, 8 (2018). https://doi.org:10.1186/s40425-018-0316-z

21 Paluch, C., Santos, A. M., Anzilotti, C., Cornall, R. J. & Davis, S. J. Immune Checkpoints as Therapeutic Targets in Autoimmunity. *Front Immunol* **9**, 2306 (2018). https://doi.org:10.3389/fimmu.2018.02306

22 Curnock, A. P. *et al.* Cell-targeted PD-1 agonists that mimic PD-L1 are potent T cell inhibitors. *JCI Insight* **6** (2021). https://doi.org:10.1172/jci.insight.152468

23 Bryan, C. M. *et al.* Computational design of a synthetic PD-1 agonist. *Proc Natl Acad Sci U S A* **118** (2021). https://doi.org:10.1073/pnas.2102164118

24 Lee, J. Y. *et al.* Structural basis of checkpoint blockade by monoclonal antibodies in cancer immunotherapy. *Nature communications* **7**, 13354 (2016). https://doi.org:10.1038/ncomms13354

25 Bardhan, K. *et al.* Phosphorylation of PD-1-Y248 is a marker of PD-1-mediated inhibitory function in human T cells. *Scientific reports* **9**, 17252 (2019). https://doi.org:10.1038/s41598-019-53463-0

26 Chemnitz, J. M., Parry, R. V., Nichols, K. E., June, C. H. & Riley, J. L. SHP-1 and SHP-2 associate with immunoreceptor tyrosine-based switch motif of programmed death 1 upon primary human T cell stimulation, but only receptor ligation prevents T cell activation. *J Immunol* **173**, 945-954 (2004). https://doi.org:10.4049/jimmunol.173.2.945

27 Patsoukis, N., Wang, Q., Strauss, L. & Boussiotis, V. A. Revisiting the PD-1 pathway. *Sci Adv* **6** (2020). https://doi.org:10.1126/sciadv.abd2712

28 Jones, B., Tite, J. P. & Janeway, C. A., Jr. Different phenotypic variants of the mouse B cell tumor A20/2J are selected by antigen- and mitogen-triggered cytotoxicity of L3T4-positive, I-A-restricted T cell clones. *J Immunol* **136**, 348-356 (1986).

29 Lu, R. M. *et al.* Development of therapeutic antibodies for the treatment of diseases. *J Biomed Sci* **27**, 1 (2020). https://doi.org:10.1186/s12929-019-0592-z

30 Tabasinezhad, M. *et al.* Trends in therapeutic antibody affinity maturation: From in-vitro towards next-generation sequencing approaches. *Immunol Lett* **212**, 106-113 (2019). https://doi.org:10.1016/j.imlet.2019.06.009

31 Chodorge, M. *et al.* A series of Fas receptor agonist antibodies that demonstrate an inverse correlation between affinity and potency. *Cell Death Differ* **19**, 1187-1195 (2012). https://doi.org:10.1038/cdd.2011.208

32 Segal, N. H. *et al.* Phase I Study of Single-Agent Utomilumab (PF-05082566), a 4-1BB/CD137 Agonist, in Patients with Advanced Cancer. *Clinical cancer research : an official journal of the American Association for Cancer Research* **24**, 1816-1823 (2018). https://doi.org:10.1158/1078-0432.CCR-17-1922

33 Rudnick, S. I. *et al.* Influence of affinity and antigen internalization on the uptake and penetration of Anti-HER2 antibodies in solid tumors. *Cancer Res* **71**, 2250-2259 (2011). https://doi.org:10.1158/0008-5472.CAN-10-2277

34 Wajant, H. Principles of antibody-mediated TNF receptor activation. *Cell Death Differ* **22**, 1727-1741 (2015). https://doi.org:10.1038/cdd.2015.109

Figure 1. Low affinity anti-CD40 mAb exhibit potent agonism in vitro. a, Left: Surface overview of CD40 – ChiLob 7/4 F(ab) complex. ChiLob 7/4 heavy (H) and light (L) chain shown in dark and light grey, respectively, bound to CD40 (blue). Mutated residues are coloured, showing their proximity to the interface. Middle: ChiLob 7/4 variable (V) region surface interface showing mutated residues as coloured and translucent. Right: ChiLob 7/4 showing interacting residues (coloured with transparent surface) in relation to CD40 (blue). Below each close up, the chain (green), residue (red), change in binding energy (purple) and DeltaG value (light blue) are shown for each mutated residue. Mutants ordered from high to low affinity. Figures created in PyMol 2.5.2. **b,** SPR of various ChiLob 7/4 m1 affinity mutants injected at 250, 50, 10, 2, 0.4, and 0 nM binding to CD40ECD. Data representative of 3 independent experiments. **c, d,** Purified hCD40Tg mouse B cells were incubated with ChiLob 7/4 m1 mutants for 2 days and surface CD23 (**c**) or CD86 (**d**) expression determined. Rightmost plots illustrate expression as a function of affinity (KD). **e,** Purified hCD40Tg mouse B cells were incubated with ChiLob 7/4 m1 mutants for 3 days and then ^{3}H-thymidine added for 18 hours to measure proliferation. Rightmost plot illustrates proliferation as a function of KD. For all experiments, means ± SEM, n = 3, data representative of 3 independent experiments.

Figure 2. Low affinity anti-CD40 mAb mediate T cell expansion and antitumor activity in vivo. **a, b,** OTI cells were adoptively transferred into hCD40Tg mice 1 day before treatment with ChiLob 7/4 m1 mutants with peripheral SIINFEKL+ CD8 cells identified by flow cytometry on day 5. (**a**) Representative dot plots, gated on CD8+ cells. (**b**) Summary OTI expansion data, Mean ± SEM, n = 8, data pooled from 2 independent experiments. Each dot, one mouse. Two-tailed, non-paired Student's t test, *p < 0.05, **p < 0.01, ***p < 0.001. p values for WT m1 vs various mutants (left to right) 0.0002, 0.0030, 0.0002, 0.0006, 0.1304. **c-e,** hCD40Tg mice were inoculated with EG7 cells. 7 days later mice received OTI cells and then 24h later ChiLob 7/4 m1 mutants. (**c**) % SIINFEKL+ CD8 cells determined on day 5. Mean ± SEM, n=17, 17, 13 (left to right), data pooled from 2-3 independent experiments. Each dot, one mouse. Two-tailed, non-paired Student's t test, p < 0.0001 for isotype vs WT m1, p = 0.0044 for WT m1 vs CDR-Y102A/Y32A m1. (**d**) Tumor size and survival. n = 13-17, data pooled from 2-3 independent experiments. Survival curves compared by log rank test, *p < 0.05, **p < 0.01, ***p < 0.001. p = 0.0006 for isotype vs WT m1, p < 0.0001 for isotype m1 vs CDR-Y102A/Y32A m1. (**e**) After the initial tumor challenge, tumor-free mice were re-inoculated with EG7 and monitored for tumor size and survival (compared by log rank test, *p < 0.05, **p < 0.01, ***p < 0.001). p = 0.0066 for isotype vs WT m1, p < 0.0002 for isotype m1 vs CDR-Y102A/Y32A m1.

Figure 3. Low affinity anti-CD40 mAb induce receptor clustering independent of FcγR. a, Jurkat-NFκB-GFP-CD40 cells were incubated with ChiLob 7/4 m1 mutants and NFκB activation (GFP) assessed. Means ± SEM, n = 3, data representative of 3 independent experiments. **b-d,** Purified hCD40Tg/FcγRnull mouse B cells were incubated with ChiLob 7/4 m1 mutants for 2 days and then assessed for surface expression of (**b**) CD23 and (**c**) CD86. Plots show affinity (KD) vs maximum CD23 or CD86 MFI. (**d**) On day 3 ^{3}H-thymidine was added to assess B cell proliferation. Means ± SEM, n = 3, data representative of 3 independent experiments. Plot shows KD vs maximum proliferation. **e-g,** Overlay of hCD40Tg (black) and hCD40Tg/FcγRnull (red) mouse B cell activation. (**e**) CD23 MFI, (**f**) CD86 MFI, and (**g**) cell proliferation. **h,** hCD40Tg/FcγRnull B cell proliferation expressed as percentage of hCD40Tg B cell proliferation. Plot shows affinity (KD) vs percent hCD40Tg B cell proliferation. **i,** Jurkat-NFκB-GFP-CD40 cells were pre-incubated with ChiLob 7/4 m1 mutants, washed and then remaining bound mAb quantified. **j,** Same experiment as (**i**) with NFκB activation (GFP) assessed. For **h-j**, Means ± SEM, n = 3, data representative of 3 independent experiments. **k,** Jurkat-CD40-GFP cells incubated with ChiLob 7/4 m1 mutants were imaged by confocal. Green: hCD40-GFP. Scale bar: 4 μm. Images representative of >15 images from 3 independent experiments. **l,** Same experiment as (**k**). Clustering index for ChiLob 7/4 m1 mutants. Means ± SEM, n = 5, data representative of 3 independent experiments. **m,** Jurkat-CD40-GFP cells incubated with ChiLob 7/4 m1 mutants were fixed and imaged by confocal. Z-stack images shown. Blue: nucleus; Green: CD40-GFP. Scale bar: 4 μm. Images representative of >10 images from 3 independent experiments.

Figure 4. Reducing affinity converts inert anti-4-1BB mAb into agonist. a, Left: Surface overview of 4-1BB-utomilumab F(ab) complex, utomilumab H (dark grey) and L (light grey) chains bound to 4-1BB (blue). Middle: Utomilumab V region surface showing mutated residues coloured and translucent. Right: Utomilumab interacting residues (coloured with transparent surface) in relation to 4-1BB (blue). Figures created in PyMol. **b,** SPR of utomilumab mutants binding to 4-1BBECD. Data representative of 3 independent experiments. **c,** Utomilumab mutants binding to 4-1BB-Jurkat cells. Means ± SEM, n=3, data representative of 3 independent experiments. **d,** Utomilumab-opsonized Ramos-4-1BB cells were incubated with hMDM to evaluate phagocytosis (ADCP). **e,** Utomilumab-opsonized IIA1.6-4-1BB cells were incubated with hPBMC to assess ADCC. For **d, e,** Means ± SEM, n=2, data representative of 3 independent experiments. **f,** Jurkat-NFκB-GFP-4-1BB cells incubated with utomilumab mutants and NFκB activation (GFP) determined. Means ± SEM, n=3, data representative of 3 independent experiments. **g,** Jurkat-4-1BB-GFP cells incubated with utomilumab, fixed and imaged by confocal. Z-stack images shown. Blue: nucleus; Green: 4-1BB-GFP. Scale bar: 4 μm. Images representative of >10 images taken from 2 independent experiments. **h,** Jurkat-4-1BB-GFP cells incubated with utomilumab and clustering index calculated. Means ± SEM, n = 5, data representative of 3 independent experiments. **i,** Same experiment as (**h**). Clustering index vs utomilumab affinity (KD). **j,** Binding of utomilumab mutant F(ab) vs IgG to Jurkat-NFκB-GFP-4-1BB cells. Data representative of 3 independent experiments. **k,** Same experiment as (**f**), NFκB activation (GFP) quantified. **l,** Same experiment as (**h**) clustering index assessed. For **k, l,** Means ± SEM, n = 3-5, Data representative of 3 independent experiments. **m,** Jurkat-NFκB-GFP-4-1BB cells incubated with utomilumab mutants, washed and then remaining bound mAb quantified. **n,** Same experiment as (**f**) NFκB activation (GFP) assessed. For **m, n,** Means ± SEM, n = 3, data representative of 3 independent experiments.

Figure 5. Reducing affinity converts an antagonistic anti-PD-1 mAb into an agonist. a, Left: Surface overview of PD-1-nivolumab F(ab) complex. Nivolumab H (dark grey) and L (light grey) chains bound to PD-1 (blue). Middle: Nivolumab V region surface showing mutated residues coloured and translucent. Right: Nivolumab interacting residues (coloured with transparent surface) in relation to PD-1 (blue). Figures created in PyMol. **b,** Jurkat-NFAT-Luc-PD-1 cells were co-cultured with CHO-OKT3-scFv-CD8α-PD-L1 cells in the presence of titrated nivolumab mutants and NFAT signalling activity assessed. Means ± SEM, n = 3, data representative of 3 independent experiments. **c,** Jurkat-NFκB-GFP-PD-1 reporter cells were incubated with nivolumab mutants and NFκB activation (GFP) assessed. Means ± SEM, n = 3, data representative of 3 independent experiments. **d,** CHO-SB2H2-scFv-CD8α cells were opsonized with OKT3 and nivolumab affinity mutants and then co-cultured with Jurkat-NFAT-Luc-PD-1 cells and NFAT activity assessed. Means ± SEM, n = 3, data representative of 3 independent experiments. One-way ANOVA followed by Kruskal-Wallis test, $p = 0.0006$. **e,** Same experiment as (**d**). CD69 expression determined. Means ± SEM, n = 3, data representative of 3 independent experiments. One-way ANOVA followed by Kruskal-Wallis test, $p < 0.0001$. **f,** Clustering index of IIA1.6-PD-1-GFP cells incubated with nivolumab mutants. Means ± SEM, n = 5, data representative of 3 independent experiments. **g,** IIA1.6-PD-1-GFP cells were incubated with nivolumab mutants, fixed and imaged using confocal. Z-stack images shown. Blue: nucleus; Green: PD-1-GFP. Scale bar: 4 μm. Images representative of >10 images from 2 independent experiments. **h,** Jurkat-NFAT-Luc-PD-1 cells were incubated with AF488-labelled nivolumab mutants at 37 ^{o}C (left) or 4^{o}C (right) and level of antibody internalization assessed as detailed in methods. Data representative of 3 independent experiments. **i,** Same experiment as (**g**). Orthogonal images shown.

Methods

Mice

hCD40 transgenic mice (hCD40Tg) were kindly provided by Professor Randolph Noelle (King's College, London)[13]. hCD40Tg/FcγR null mice (hCD40Tg/*Fcer1g*$^{-/-}$/*FcγR2b*$^{-/-}$) were generated as described previously by first breeding *Fcer1g*$^{-/-}$ and *FcγR2b*$^{-/-}$ mice to generate homozygous FcγR null mice (*Fcer1g*$^{-/-}$ x *FcγR2b*$^{-/-}$) and homozygous FcγR null mice were subsequently crossed with hCD40Tg mice[15]. All mice were bred in-house and maintained on a 12 hour light/dark cycle, food and water were provided ad libitum and temperature was maintained between 20-24°C with 55 (+/-15) % humidity. Mice were checked daily to ensure healthy status. All experiments were conducted under UK Home Office licence numbers PB24EEE31, P4D9C89EA, P540CBA98, and P39FE2AA7 and according to local ethical committee guidelines.

Human Samples

Human PBMCs were derived from blood cones collected from healthy donors through Southampton National Blood Services with prior informed consent. The use of human blood was approved by the East of Scotland Research Ethics Service, Tayside, UK.

Cell lines

Wild type Ramos, CHO-k1, EG7, A20 and Jurkat cells were obtained from ATCC. IIA1.6 cells were used as previously described[35]. Wild type Jurkat-NFκB-GFP reporter cell line was from System Biosciences, USA. Wild type Jurkat-NFAT-Luc reporter cell line was from Promega, UK. All cell lines were maintained in a humidified incubator at 37ºC and 5% CO_2, and cultured in RPMI media supplemented with 10% heat-inactivated FBS, 2mM L-glutamine, 1mM pyruvate, 100U/mL penicillin, 100 µg/mL streptomycin and 50 µM β-mercaptoethanol (complete RPMI media, all from Thermofisher), with the exception of CHO-k1 cells which were cultured without β-mercaptoethanol.

Generation of affinity mutants

Models of F(ab)-receptor complexes were obtained from the PDB (accession codes: 6FAX – ChiLob 7/4:CD40, 6MI2 – Utomilumab:4-1BB, 5WT9 – Nivolumab:PD-1). To identify potential interacting residues, the models were analysed in PISA using the QtPISA interface[36,37]. Potential mutants were generated by mutating the potential interacting residues identified by PISA to alanine in PyMol 2.5.2. using the mutation wizard. Each mutant was subsequently analysed in PISA. The resulting difference in the value of deltaG and binding energy from the wild type structure were recorded and used to predict effect on binding affinity. To generate double mutants, a confusion matrix of the difference in deltaG and binding energy from wild type was used to give combined mutation scores. Decisions on which mutants to produce were based on the scores in the confusion matrix and the proximity of the residue to the binding interface. Humanization was performed and resulting sequences were kindly provided by Glycotope GmbH, Berlin, Germany.

Antibodies and Reagents

All antibodies were produced in the ExpiCHO system as previously described[15]. The variable domain sequence for Utomilumab (WO2015/119923A1), Nivolumab (WO2006/121168), Varlilumab (US9169325), TGN1412 (US7585960B2) and OKT3[38] were derived from published sequences. The light and heavy chain variable domain sequences were synthesized by GeneArt and subcloned into **pEE12.4** and **pEE6.4** expression vectors, respectively (Lonza, UK) encoding the constant domain of different IgG isotypes. The CDR mutations for ChiLob 7/4, Utomilumab and Nivolumab were achieved by site-directed mutagenesis using the QuickChange Site-Directed Mutagenesis Kit (Agilent, UK). Plasmids encoding the heavy and light chains were transiently transfected into ExpiCHO cells for 10 days before the supernatant was harvested and antibodies were purified on a MabSelect SuRe column (GE healthcare, UK). All antibody preparations were checked by HPLC to contain < 1% aggregate and by Endosafe-PTS portable test (Charles River Laboratories, L'Arbresle, France) to contain < 5EU endotoxin/mg antibody.

The DNA constructs containing CD40-GFP and 4-1BB-GFP were generated as previously described[17]. The PD-1-GFP construct was generated by subcloning human PD-1 (Accession U64863) into pcDNA3 plasmid containing the GFP fragment at the C-terminus. The OKT3-scFv-CD8α DNA construct was

591 designed as VL-(G4S)3-VH-CD8α with an EcoRI restriction site between the VH and CD8α and cloned
592 into the **pCIpuro** vector. The variable domain sequence of the anti-human IgG Fc mAb SB2H2 was
593 obtained from the hybridoma by sequencing the cDNA generated using the MMLV reverse
594 transcriptase and a universal primer as described previously[39]. The SB2H2-scFv-CD8α DNA construct
595 was designed as VL-(G4S)3-VH-CD8α with an EcoRI restriction site between the VH and CD8α and
596 cloned into the **pcDNA3** vector. Human PD-L1 (Accession NM_014143) was cloned into the **pcDNA3**
597 vector.

598 Recombinant soluble trimeric CD40L and 4-1BBL were produced in-house as previously described[17].
599 Fab fragments of mouse IgG1 anti-CD40 mAb was generated using the Pierce Mouse IgG1 Fab and
600 $F(ab')_2$ Preparation Kit (Thermofisher). The Fab fragment of human IgG4 anti-4-1BB mAb was
601 generated using immobilized papain (Thermofisher).

602 **Surface plasmon resonance**

603 A Biacore T200 instrument was used throughout. Recombinant extracellular domains of human CD40
604 (R and D systems), 4-1BB (R and D systems), PD-1 (R and D systems), TNFRII (R and D systems),
605 CD27 (in-house) and CD28 (Biolegend) were immobilized onto a CM5 chip by amine-coupling
606 chemistry. To compare the binding affinity of various target-specific mAb mutants and natural soluble
607 ligands towards their respective receptor or homologue, mAb and ligand were injected through the flow
608 cell at 250, 50, 10, 2, 0.4, and 0 nM in HBS-EP+ running buffer at a flow rate of 30 mL per minute,
609 allowing 300 seconds for association and 300 seconds for dissociation. Data were collected using
610 Biacore T200 control software. The sensorgrams were fitted with bivalent analyte model and the Ka
611 and Kd values were calculated using the Biacore Bioevaluation software; the KD values were calculated
612 as Kd/Ka. All SPR reagents and software were from GE healthcare, UK.

613 **Assessment of antibody cell surface receptor binding**

614 To assess the level of antibody binding to cells expressing human CD40, 4-1BB or PD-1, relevant cells
615 were incubated with various concentrations of anti-CD40, anti-4-1BB or anti-PD-1 mAb as indicated
616 in figure legends for 30 minutes at 4^{o}C and then unbound mAb were washed off using FACS wash

buffer (PBS, 1% BSA, 0.01% sodium azide) and PE-conjugated polyclonal goat $F(ab')_2$ secondary anti-human Fc (1/200) or PE-conjugated polyclonal goat $F(ab')_2$ secondary anti-mouse Fc (1/200, both from Abcam, UK) were added for 30 minutes at 4°C and then unbound mAb washed off using FACS wash. To detect the level of bound Fab fragment, FITC-conjugated anti-mouse IgG Fab (1/100) or AF647-conjugated anti-human IgG kappa light chain (1/100) was used depending on the mAb isotype. The level of bound mAb was quantified by flow cytometry.

Competitive cell surface receptor binding

For competitive cell binding assay, Ramos cells were co-incubated with a fixed concentration of AF647-labelled ChiLob 7/4 hIgG1 (0.5 μg/mL) and various concentrations of competing ChiLob 7/4 mIgG1 or ChiLob 7/4 hIgG2 affinity mutants for 30 minutes, cells were then washed and the level of AF647-labelled ChiLob 7/4 hIgG1 remaining bound to the cell surface was quantified by flow cytometry.

Flow cytometry

Flow cytometry experiments were conducted using FACSCalibur, FACSCanto II or FACSMelody (all from BD Biosciences). Flow cytometry data were collected using BD CellQuest and BD FACSDIVA software and data analysis was performed using FCS Express software Version 3 (De Novo Software) or Flowjo (BD).

B cell activation assay

Human B cells were purified from human PBMC using the MojoSort Human B Cell Isolation Kit (Biolegend, UK) and mouse B cells were purified from splenocytes using the MojoSort Mouse Pan B Cell Isolation Kit (Biolegend, UK). Purified B cells were incubated with various anti-CD40 mAb as indicated in figure legends for 2 days and imaged using a conventional light microscope (Olympus CKX41), then assessed for CD23 (anti-CD23, 1/160) and CD86 (anti-CD86, 1/100) expression using flow cytometry. To assess B cell proliferation, ^{3}H thymidine (Perkin Elmer) was added at 1 μCi per well on day 3 for an additional 18 hours as previously[15].

642 **OTI expansion assay**

643 OTI expansion assay was performed as previously described[15]. To assess the ability of anti-CD40 mAb
644 to induce OTI T cell expansion, $1x10^5$ OTI cells were injected intravenously into CD40KOTg mice one
645 day before the injection of 100 µg OVA in combination with 25 µg or 500 µg of various anti-CD40
646 mAb intravenously. Mice were then bled 4-5 days later as indicated in figure legends, and the level of
647 OTI expansion was assessed by the proportion of CD8+ SIINFEKL tetramer positive cells by flow
648 cytometry.

649 **EG7 tumor therapy**

650 The EG7 model was performed as previously described[15]. Briefly, mice were inoculated with $5x10^5$
651 EG7 cells subcutaneously and then treated with 25 µg anti-CD40 mAb and 100 µg OVA intravenously
652 when the sum of tumor length and width reached approximately 10 mm. Tumor size was measured 3
653 times per week using digital calipers and mice were culled when the sum of tumor length and width
654 reached 30 mm or when the general health of the mice reached humane end-point criteria. For
655 rechallenge, tumor-free mice were inoculated with $5x10^5$ EG7 cells subcutaneously and monitored for
656 tumor growth as above. Tumor volume was calculated using the formula: $V = (W^2 \times L)/2$ where W is
657 tumor width and L is tumor length.

658 **Human dendritic cell activation and mixed leukocyte reaction**

659 Human immature DCs were generated as previously described[40]. Briefly, CD14+ monocytes were
660 isolated from human PBMC using a magnetic negative selection kit (Miltenyi Biotech, UK) and then
661 cultured in the presence of 500 IU/mL IL-4 and 1000 IU/mL GM-CSF (both cytokines produced in-
662 house) for 5 to 6 days. The identity of DC was confirmed by CD11c (anti-CD11c, 1/20) and DC-SIGN
663 (anti-CD209, 1/20) expression. For direct stimulation, immature DCs were treated with 50 µg/mL anti-
664 CD40 mAb for 2 days and the level of CD86 expression (anti-CD86, 1/20) was quantified by flow
665 cytometry. A mixed leukocyte reaction was performed as previously described[15]. Briefly, varying
666 numbers of immature DCs were first treated with 50 µg/mL anti-CD40 mAb for 2 days and then washed
667 and further incubated with $0.1x10^6$ purified human allogeneic CD4+ T cells (MojoSort Human CD4 T

Cell Isolation Kit, Biolegend, UK) for 4 days. ^{3}H thymidine was added at 1 µCi per well on day 4 for an additional 18 hours to assess T cell proliferation.

Human PBMC peptide recall assay

The expansion of antigen-specific T cells within PBMC was achieved using CEFX Ultra SuperStim Pool (JPT Peptide Technologies, Germany) that contains a pool of 176 known peptides based on different infectious agents that have been shown to induce antigen-specific T cell expansion[41,42]. Briefly, fresh human PBMCs were labelled with 2 µM CFSE (Thermofisher) in PBS and then $0.2x10^{6}$ PBMCs were incubated with 50 µg/mL anti-CD40 mAb and 0.6 µM CEFX Ultra SuperStim Pool for 5 days to recall antigen-responsive CD8+ T cells. The proliferating cells expressing CD3 (anti-CD3, 1/20) and CD8 (anti-CD8, 1/20) were regarded as antigen-responsive cells and their level of activation was measured by CD25 expression (anti-CD25, 1/20) on day 5 by flow cytometry.

NFκB assay

pCIpuro vector encoding CD40, 4-1BB (expressing the hCD40 intracellular signalling domain) or PD-1 (expressing the CD40 transmembrane and intracellular signalling domain) was transfected into Jurkat-NFκB-GFP cells and stable clones were selected using 1 µg/mL puromycin. To examine NFκB activation, cells stably transfected with each receptor were incubated with relevant mAb as indicated in each legend for 6 hours at 37^{o}C and the level of NFκB activation was subsequently quantified by GFP fluorescence assessed using flow cytometry.

Assays to evaluate the impact of receptor density on mAb agonism

Jurkat-NFκB-GFP cells stably transfected with CD40, 4-1BB or PD-1 were first sorted into populations expressing low, medium and high levels of respective receptor using the FACSMelody (BD). Cells were then treated with various mAb as indicated for 6 hours at 37^{o}C and the level of NFκB activation was subsequently quantified by GFP fluorescence assessed using flow cytometry. Receptor quantification was performed using the Quantum Alexa Fluor 647 MESF kit (Bangs Laboratories). To quantify the level of PD-1 expression on human primary T cells, human PBMC were activated with Immunocult (Stemcell Technologies) for 2 days and then CD3+ T cells were analysed for PD-1

expression by flow cytometry. To assess the level of 4-1BB expression on human primary CD8+ T cells, CD8+ T cells were purified from human PBMC using the MojoSort Human CD8 T Cell Isolation Kit (Biolegend) and then activated with plate-bound anti-CD3 (clone OKT3) and anti-CD28 (clone TGN1412) (both produced in-house) for 24 hours before 4-1BB quantification by flow cytometry.

Assays to evaluate the effect of antibody concentration on mAb agonism

Jurkat-NFκB-GFP cells stably transfected with CD40, 4-1BB or PD-1 were treated with 50 µg/mL mAb as indicated for 30 minutes at room temperature and then excess unbound mAb was washed off. Cells were then incubated at 37ºC for various periods as indicated and the level of mAb remaining bound to the cell surface was quantified by DL650-conjugated goat $F(ab')_2$ secondary anti-mouse Fc (1/200) or by DL650-conjugated goat $F(ab')_2$ secondary anti-human Fc (1/200, both from Abcam) using flow cytometry. The level of NFκB activation was concurrently quantified by GFP fluorescence assessed using flow cytometry.

Confocal Microscopy

DNA encoding CD40ECD-GFP and 4-1BBECD-GFP were sub-cloned into **pCIpuro** vector and transfected into Jurkat cells using the Nucleofector Kit V (Lonza). Stable Jurkat clones were selected using 1 µg/mL puromycin. IIA1.6 cells stably transfected with full length PD-1-GFP (IIA1.6-PD-1-GFP) were generated by transfecting IIA1.6 cells with pCIpuro plasmid encoding PD-1-GFP using nucleofection Kit V (Lonza) and stable clones were selected using 4 µg/mL puromycin. Confocal microscopy was performed as previously described[17]. Jurkat cells were incubated with respective 50 µg/mL mAb for three hours at 37ºC and then fixed with cold methanol on ice for 10 minutes before the nucleus was stained with DAPI (Thermofisher). Alternatively, cells were fixed with 2% paraformaldehyde (PFA; Thermofisher) at room temperature for 10 minutes before the nucleus was stained with DAPI. For live cell imaging, cells were imaged directly without fixation. Confocal images were acquired using a Leica SP8 confocal microscope and data were analysed using Leica Application Suite X (all from Leica). In order to measure receptor clustering at the cell:cell junctions in relation to the periphery of the cells, a clustering index was calculated (Extended data Fig. 7a). Confocal images

through the centre of the cells were opened in Leica Application Suite X software (Leica) and fluorescence intensity measurements were taken for regions of interest (ROI) at the cell:cell junctions or at the periphery of the cells (non-contacting membrane); these were determined by eye with cell periphery measurements taken for each corresponding cell:cell junction i.e. two cell periphery ROI's would be collected for a cell that contained two cell:cell cluster ROI's. A clustering index was calculated for five confocal images with up to five cell:cell clusters per image for each treatment. An average clustering index was calculated from five confocal images with up to five cell to cell clusters per image for each treatment. The clustering index designates the ratio of fluorescence intensity at the cell:cell junction over the fluorescence intensity at the cell periphery calculated using Leica Application Suite X software (Leica). A larger clustering index denotes higher levels of receptor clustering. Circularity of the cells was measured in ImageJ where a circularity value of 1.0 indicates a perfect circle (circularity = 4π (area/perimeter^2). Confocal images through the centre of the cells were opened in ImageJ, an ROI was manually drawn around individual cells following the membrane and the circularity measured. Cell circularity was measured for five confocal images for each treatment and the results of three independent experiments were pooled.

Direct stochastic optical reconstruction microscopy (dSTORM)

IBIDI glass-bottom chambers were first coated with poly-D-lysine (Sigma). Jurkat cells expressing CD40ECD-GFP were incubated with 25 µg/mL anti-CD40 or CD40L at 37 °C for 1 hour and then washed with PBS and fixed with 4% PFA. GFP was detected using AF647-conjugated anti-GFP nanobodies (Proteintech Europe, 1/500) following the manufacturer's instructions. TCEP STORM buffer comprises 3 solutions: Solution A: 1 µg/mL Catalase, 0.2 mM TCEP, 2.5% glycerol, 1.25 mM KCl, 1 mM Tris-HCl, 50 µg /mL glucose oxidase. Solution B: 40 mg/mL glucose, 4% glycerol. Solution C: 0.1 M MEA-HCl. Immediately before dSTORM collection, the TCEP STORM buffer solutions A (50 µL), B (400 µL), C (100 µL) and PBS (450 µL) were mixed and then added to the well. A wide field fluorescence reference image was acquired before dSTORM images (10,000 frames, 30 ms exposure) were collected using the ONI Nanoimager equipped with a 640 nm laser and NimOS1.6 software (ONI, UK). Analysis of dSTORM data was carried out using the CODI cloud analysis platform

(beta version, ONI, UK). Images were subjected to drift correction and filtering before ROI's were drawn around the cell:cell junctions. For CD40L, ROI's were also drawn around large clusters present outside of the cell:cell junctions. Localisations within the ROI's were identified and grouped into sub-clusters using HDBSCAN81. The following features were extracted for each individual subcluster: number of localisations; density (localisations/area) and area (computed from the convex hull of the cluster).

In vitro assessment of receptor internalization

The level of CD40 and PD-1 internalization was quantified using a fluorescence quenching assay as described before[43]. To assess CD40 internalization, AF488-labelled anti-CD40 mAb or AF488-labelled anti-CD20 ritxuimab hIgG2 were added to Ramos cells as indicated for 10, 30, 60, 120 or 180 minutes at 4ºC or 37 ºC. To assess PD-1 internalization, AF488-labelled anti-PD-1 mAb or the anti-CD3 OKT3 hIgG1 pre-opsonized with AF488-labelled anti-human IgG Fc mAb SB2H2 (produced in-house) were added to Jurkat-NFAT-Luc-PD-1 cells as indicated for 10, 30, 60, 120 or 180 minutes at 4ºC or 37 ºC. Following that, Ramos or Jurkat-NFAT-Luc-PD-1 cells were washed and half the cells treated with anti-AF488 antibody (Thermofisher, 1/100) at 4ºC that quenches AF488 fluorescence. The remaining unquenched AF488 fluorescence analysed by flow cytometry correlates to internalized CD40 or PD-1. % Total Expression quantifies remaining cell surface-bound receptor and was calculated as % (unquenched fluorescence – quenched fluorescence)/(unquenched fluorescence).

Antibody-dependent cellular phagocytosis (ADCP)

Ramos cells stably transfected with 4-1BBECD-Tm (Ramos-4-1BB) were generated by transfecting Ramos cells with **pcDNA3** plasmid encoding 4-1BBECD-Tm using nucleofection Kit V (Lonza) and stable clones were selected using 1 mg/mL geneticin (Extended Data Fig. 10c). Antibody-dependent cellular phagocytosis was performed as previously described[17], using Ramos-4-1BB as target cells and human monocyte derived macrophages (hMDM) as the effector cells. The hMDM were derived by culturing monocytes in the presence of 100 ng/ml M-CSF (in-house) for 6 days. The day before the phagocytosis assay, $1x10^5$ hMDM were plated onto a 96 flat bottom plate (Thermofisher). The next

day, target Ramos-4-1BB cells were labelled with CFSE followed by opsonisation with various anti-4-1BB mAb as indicated in the figure legend for 30 minutes at 4°C. $5x10^5$ target cells were then added to each well and incubated at 37°C for 30 minutes for phagocytosis to occur. The samples were subsequently stained with anti-CD14-APC (1/20) to identify hMDM, and cells positive for both CFSE and CD14 as assessed by flow cytometry were classified as hMDM that had undergone phagocytosis. % ADCP was calculated as: (CFSE+CD14+ cells)/(Total CD14+ cells) x 100.

Antibody-dependent cellular cytotoxicity (ADCC)

IIA1.6 cells stably transfected with full length human 4-1BB (IIA1.6-4-1BB) were generated by transfecting IIA1.6 cells with **pCIpuro** plasmid encoding human 4-1BB using nucleofection Kit V (Lonza) and stable clones were selected using 4 µg/mL puromycin (Extended Data Fig. 10d). Antibody-dependent cellular cytotoxicity was performed as previously described[44], using IIA1.6-4-1BB cells as targets and human PBMC as effector cells. Briefly, target cells were labelled with Calcein-AM (Thermofisher), added to wells of a 96-well round bottom plate (Thermofisher) at $8x10^5$ per well and then incubated with various anti-4-1BB mAb as specified in the figure legend for 30 minutes at 4°C. $4x10^6$ effector cells were then added to each well and incubated at 37°C for 4 hours before cells were centrifuged and the supernatant quantified for Calcein-AM fluorescence using a Varioskan Flash plate reader (Thermofisher). The control wells for maximal lysis contained 4% Triton X-100 (Sigma). The level of ADCC was expressed as % of maximal lysis = (experimental fluorescence – background fluorescence)/(maximal lysis – background fluorescence) x 100.

PD-1 blockade assay

Jurkat-NFAT-Luc-PD-1 cells were generated by transfecting wild type Jurkat-NFAT-Luc cells (Promega) with **pcDNA3** plasmid encoding human PD-1 using nucleofection Kit V (Lonza) and stable clones were selected using 1 mg/mL geneticin. CHO-OKT3-scFv-CD8α-PD-L1 cells were generated by co-transfecting CHO-k1 cells with **pCIpuro** vector encoding OKT3-scFv-CD8α and **pcDNA3** vector encoding human PD-L1 and selecting stable clones using 10 µg/mL puromycin and 1 mg/mL geneticin. To assess the ability of anti-PD-1 mAb to block the PD-1/PD-L1 interaction, $5x10^4$ CHO-

OKT3-scFv-CD8α-PD-L1 cells were plated onto wells of sterile White Opaque 96-well Microplates (Perkin Elmer, UK) overnight; the next day, $5x10^4$ Jurkat-NFAT-Luc-PD-1 cells were added to each well along with the various anti-PD-1 mAb as indicated in each figure legend for 6 hours before the ONE-Glo Reagent (Promega) was added and luciferase activity was read using the Varioskan Flash plate reader (Thermofisher).

PD-1-mediated T cell suppression assay

CHO-k1 cells stably transfected with SB2H2-scFv-CD8α (CHO-SB2H2-scFv-CD8α) were generated by transfecting WT CHO-k1 cells with **pcDNA3** plasmid encoding SB2H2-scFv-CD8α using GenePorter (Amsbio, UK). Stable clones were selected using 1 mg/mL geneticin. For the PD-1-mediated T cell suppression assay, CHO-SB2H2-scFv-CD8α cells were first co-incubated with 20 µg/mL nivolumab variants and 5 µg/mL OKT3 hIgG1 for 30 minutes before excess unbound mAb was washed off using complete RPMI media. Jurkat-NFAT-Luc-PD-1 cells were then added to the opsonized CHO-SB2H2-scFv-CD8α cells and incubated for 6 hours. CD69 expression (anti-CD69, 1/20) on Jurkat-NFAT-Luc-PD-1 cells was measured by flow cytometry and the level of NFAT activation was quantified by measuring the luciferase activity using the ONE-Glo Reagent (Promega) as above.

Statistics and Reproducibility

Data analysis was performed using GraphPad Prism 9.2.0 (GraphPad Software). Two-tailed, non-paired Student t test was used for pairwise comparisons. One-way ANOVA followed by Kruskal-Wallis test was used for multiple comparisons as specified in figure legends. Throughout $*p < 0.05$, $**p < 0.01$, $***p < 0.001$, n.s., not significant. Reproducibility including technical replicates and independent biological experiments are stated in each figure legend.

Data availability

Original raw data will be provided upon request to include all supporting information. Source data are provided with this paper. ChiLob 7/4 : CD40 complex – PDB: 6FAX (DOI: 10.2210/pdb6FAX/pdb).

Utomilumab : 4-1BB complex – PDB: 6MI2 (DOI: 10.2210/pdb6MI2/pdb). Nivolumab : PD-1 complex – PDB: 5WT9 (DOI: 10.2210/pdb5WT9/pdb).

Additional References

35 Roghanian, A. *et al.* Antagonistic human FcgammaRIIB (CD32B) antibodies have anti-tumor activity and overcome resistance to antibody therapy in vivo. *Cancer cell* **27**, 473-488 (2015). https://doi.org:10.1016/j.ccell.2015.03.005

36 Krissinel, E. Stock-based detection of protein oligomeric states in jsPISA. *Nucleic Acids Res* **43**, W314-319 (2015). https://doi.org:10.1093/nar/gkv314

37 Krissinel, E. & Henrick, K. Inference of macromolecular assemblies from crystalline state. *J Mol Biol* **372**, 774-797 (2007). https://doi.org:10.1016/j.jmb.2007.05.022

38 Arakawa, F. *et al.* Cloning and sequencing of the VH and V kappa genes of an anti-CD3 monoclonal antibody, and construction of a mouse/human chimeric antibody. *Journal of biochemistry* **120**, 657-662 (1996). https://doi.org:10.1093/oxfordjournals.jbchem.a021462

39 Meyer, L. *et al.* A simplified workflow for monoclonal antibody sequencing. *PLoS One* **14**, e0218717 (2019). https://doi.org:10.1371/journal.pone.0218717

40 Sallusto, F. & Lanzavecchia, A. Efficient presentation of soluble antigen by cultured human dendritic cells is maintained by granulocyte/macrophage colony-stimulating factor plus interleukin 4 and downregulated by tumor necrosis factor alpha. *J Exp Med* **179**, 1109-1118 (1994). https://doi.org:10.1084/jem.179.4.1109

41 Gate, D. *et al.* Clonally expanded CD8 T cells patrol the cerebrospinal fluid in Alzheimer's disease. *Nature* **577**, 399-404 (2020). https://doi.org:10.1038/s41586-019-1895-7

42 Fernandes, R. A. *et al.* Immune receptor inhibition through enforced phosphatase recruitment. *Nature* **586**, 779-784 (2020). https://doi.org:10.1038/s41586-020-2851-2

43 Austin, C. D. *et al.* Endocytosis and sorting of ErbB2 and the site of action of cancer therapeutics trastuzumab and geldanamycin. *Mol Biol Cell* **15**, 5268-5282 (2004). https://doi.org:10.1091/mbc.e04-07-0591

44 Sopp, J. M. *et al.* On-target IgG hexamerisation driven by a C-terminal IgM tail-piece fusion variant confers augmented complement activation. *Commun Biol* **4**, 1031 (2021). https://doi.org:10.1038/s42003-021-02513-3

Acknowledgments

We would like to thank the pre-clinical unit staff for animal husbandry. We thank Dr David Johnston from the Biomedical Imaging Unit, Southampton General Hospital, Southampton UK for assistance with confocal microscopy. We thank Dr Deirdre Kavanagh from the University of Oxford for sharing the dSTORM buffer recipe, and Dr James Felce from ONI, Oxford, UK for advice on dSTORM data analysis. The dSTORM microscopy was made possible through the generous funding of an ONI Nanoimager by the Mark Benevolent Fund. Funding was provided by CRUK grants A20537, A25139,

A25169 and DRCDDRPGM-Apr2020\100005. X.Y. is funded by a Careertrack Fellowship provided by the Faculty of Medicine in conjunction with the Cancer Immunology Talent fund.

Author Contributions

X.Y. designed and performed the experiments, analyzed and interpreted data, and wrote the manuscript. C.O., H.T.C., S.J., C.P., J.K., K.L.C., T.I. and I.M. generated or provided key reagents or performed and analyzed the experiments. J.W.E and I.T supported acquisition of funding and contributed to the conception of the work and approach. M.J.G. designed the study, discussed and interpreted data. M.S.C. designed the study, supervised data collection, discussed and interpreted data and wrote the manuscript with X.Y. All authors commented upon and approved the final manuscript.

Competing interests

Mark S. Cragg acts as a consultant for a number of biotech companies, being retained as a consultant for BioInvent and has received research funding from BioInvent, GSK, UCB, iTeos, and Roche and receives institutional payments and royalties from patents and licenses relating to antibody immunotherapy. No other authors have any conflicts of interest.

Extended Data Figure 1. Characterization of anti-CD40 mIgG1 mAb ChiLob 7/4 affinity mutants. **a,** SPR of various ChiLob 7/4 m1 affinity mutants injected at 250, 50, 10, 2, 0.4, and 0 nM binding to CD40ECD. Data representative of 3 independent experiments. **b,** ChiLob 7/4 m1 affinity mutants were evaluated for their binding affinity for CD40ECD by SPR as indicated in **a**, with affinity constants (ka, kd and KD) calculated. Fold change indicates affinity change compared with WT ChiLob 7/4 m1. **c,** Ramos cells were incubated with 0.5 μg/mL of AF647-labelled ChiLob 7/4 h1 and various concentrations of competing ChiLob 7/4 m1 affinity mutants as indicated and then washed and bound AF647-labelled ChiLob 7/4 h1 detected. Means ± SEM, n = 3, data representative of 3 independent experiments.

Extended Data Figure 2. Low affinity anti-CD40 mIgG1 mAb exhibit potent agonism. a, Purified hCD40Tg mouse B cells were incubated with ChiLob 7/4 m1 mutants for 2 days and then stained for surface expression of CD23. Left plot, exemplar raw data. **b,** Same experiment as (**a**). Surface expression of CD86. Left plot, exemplar raw data. **c,** Purified hCD40Tg mouse B cells were incubated with ChiLob 7/4 m1 mutants for 3 days and then ^{3}H-thymidine was added for 18 hours to measure proliferation. Inset cell culture images were taken on day 2. Scale bar, 0.5 mm. For (**a-c**), Means ± SEM, n = 3, data representative of 3 independent experiments. Rightmost plots illustrate the CD23 expression, CD86 expression or proliferation as a function of the on-rate (ka) or off-rate (kd). **d,** hCD40Tg mice were inoculated with EG7 cells. 7 days later, mice received OTI cells and the next day were treated with ChiLob 7/4 m1 mutants as indicated. Tumor growth curves are shown with numbers as proportion of tumour free mice at experiment end inset. n = 13-17, data pooled from two to three independent experiments.

Extended Data Figure 3. Characterization of anti-CD40 hIgG2 mAb ChiLob 7/4 affinity mutants. a, SPR of various ChiLob 7/4 h2 affinity mutants injected at 250, 50, 10, 2, 0.4, and 0 nM binding to CD40ECD. Data representative of 3 independent experiments. **b,** ChiLob 7/4 h2 affinity mutants were evaluated for their binding affinity for CD40ECD by SPR as indicated in **a**, with affinity constants (ka, kd and KD) calculated. Fold change indicates affinity change compared with WT ChiLob 7/4 h2. **c,** Ramos cells were incubated with 0.5 μg/mL of AF647-labelled ChiLob 7/4 h1 and various concentrations of competing ChiLob 7/4 h2 affinity mutants as indicated and then washed and bound AF647-labelled ChiLob 7/4 h1 detected. Means ± SEM, n = 3, data representative of 3 independent experiments. **d, e,** Purified hCD40Tg mouse B cells were incubated with ChiLob 7/4 h2 affinity mutants as indicated for 2 days and then stained for surface expression of CD23 (**d**, left plot, exemplar raw data) and CD86 (**d**, right plot, exemplar raw data). B cell proliferation was assessed by ^{3}H-thymidine incorporation (**e**). Plots show affinity (KD) vs maximum CD23 MFI, maximum CD86 MFI or maximum proliferation. Means ± SEM, n = 3, data representative of 3 independent experiments. **f,** OTI cells were adoptively transferred into hCD40Tg mice 1 day before treatment with ChiLob 7/4 h2 mutants with

peripheral SIINFEKL+ CD8 cells identified by flow cytometry on day 4. Mean ± SEM, n = 7, data pooled from two independent experiments. Each dot represents one mouse. Two-tailed, non-paired Student's t test, the p values for WT h2 vs FW-12 h2, vs FW-22 h2, vs FW-16 h2 are (from left to right) 0.0023, 0.0023 and 0.0023. **g,** Purified human B cells were incubated with ChiLob 7/4 h2 affinity mutants for 2 days and then stained for surface expression of CD23 (left plot, exemplar raw data) and CD86 (right plot, exemplar raw data). **h,** Purified human B cells were incubated with ChiLob 7/4 h2 mutants as indicated for 3 days and then ^{3}H-thymidine was added for 18 hours to measure proliferation. Inset cell culture images were taken on day 2. For **g, h,** Means ± SEM, n = 3, data representative of 3 independent experiments. **i**, Purified human B cells were incubated with ChiLob 7/4 h2 affinity mutants as indicated for 2 days**.** B cell proliferation was assessed by ^{3}H-thymidine incorporation. Plots show affinity (KD) vs maximum CD23 MFI, maximum CD86 MFI or maximum proliferation. Means ± SEM, n = 3, data representative of 3 independent experiments.

Extended Data Figure 4. Low affinity anti-CD40 mAb exhibit potent agonism in human systems. **a,** Human DCs were stimulated with various ChiLob 7/4 h2 affinity mutants for 2 days and then evaluated for CD86 expression. The ranking of CD86 MFI was plotted against KD. Means ± SEM, each dot represents an average value from 9 donors. **b,** Gating strategy and representative histograms for **a**. **c,** Human DCs were pre-treated with ChiLob 7/4 h2 affinity mutants for 2 days and co-cultured with allogeneic CD4+ T cells for 5 days. CD4+ T cell proliferation was measured by ^{3}H-thymidine incorporation. Ranking of CD4+ T cell proliferation was plotted against affinity (KD). Means ± SEM, each dot represents the average from 7 donors. **d,** Human monocyte-derived DCs were pre-treated with ChiLob 7/4 h2 affinity mutants for 2 days and then co-cultured with allogeneic CD4+ T cells at different ratios for 5 days. CD4+ T cell proliferation was measured by ^{3}H-thymidine incorporation. The ranking of CD4+ T cell proliferation was plotted against affinity (KD). Means ± SEM, each dot represents the average value from 7 healthy donors. **e,** CFSE-labelled PBMCs were stimulated with antigenic peptides and ChiLob 7/4 h2 affinity mutants for 5 days and proliferating CD8+ T cells evaluated for surface expression of CD25. Ranking of CD25 MFI plotted against KD. Means ± SEM, each dot represents the

939 average from 8 donors. **f,** Gating strategy and representative histograms for CD25 expression of
940 proliferating CD8+ T cells in PBMCs stimulated with CEFX Ultra SuperStim Pool and ChiLob 7/4 h2
941 affinity mutants. Data representative of 8 donors.

942

943 **Extended Data Figure 5. Low affinity anti-CD40 mIgG1 mAb induce agonism independent of**
944 **FcγR. a,** Jurkat-NFκB-GFP-CD40 reporter cells were incubated with various ChiLob 7/4 m1 affinity
945 mutants for 6 hours and the level of NFκB activation (GFP) assessed. Means ± SEM, n = 3, data
946 representative of 3 independent experiments. Representative flow data shown in left panels.
947 Subsequent plots reflect the dose-response for the different mAb followed by cumulative plots of the
948 data as a function of affinity parameters; ka (top) and kd (bottom), respectively. **b-d,** Purified
949 hCD40Tg/FcγRnull mouse B cells were incubated with ChiLob 7/4 m1 mutants for 2 days and then
950 stained for surface expression of (**b**) CD23 and (**c**) CD86. Representative flow data shown in left
951 panels. Subsequent plots reflect the dose-response for the different mAb followed by cumulative plots
952 of the data as a function of affinity parameters; ka (top) and kd (bottom), respectively.(**d**) On day 3
953 ^{3}H-thymidine was added for 18 hours to assess B cell proliferation. Inset cell culture images were
954 taken on day 2. Means ± SEM, n = 3, data representative of 3 independent experiments. Scale bar, 0.5
955 mm. Plots reflect the dose-response for the different mAb followed by cumulative plots of the data as
956 a function of affinity parameters; ka (top) and kd (bottom), respectively.

957

958 **Extended Data Figure 6. Low affinity anti-CD40 hIgG2 mAb induce agonism independent of**
959 **FcγR. a-c,** Purified hCD40Tg/FcγRnull mouse B cells were incubated with ChiLob 7/4 h2 mutants
960 for 2 days and then stained for surface expression of (**a**) CD23 and (**b**) CD86. Representative flow
961 data shown in left panels. Subsequent plots reflect the dose-response for the different mAb followed
962 by cumulative plots of the data as a function of affinity (KD). (**c**) On day 3 ^{3}H-thymidine was added
963 for 18 hours to assess B cell proliferation. Inset cell culture images were taken on day 2. Means ±
964 SEM, n = 3, data representative of 3 independent experiments. Scale bar, 0.5 mm. Plots reflect the

dose-response for the different mAb followed by cumulative plots of the data as a function of affinity (KD).

Extended Data Figure 7. Low affinity anti-CD40 mAb induce agonism through receptor clustering with minimal receptor internalization. a, Schematic of the method for calculating clustering index. Confocal images through the centre of cells were opened in LAS X software and fluorescence intensity measurements taken for regions of interest at the cell:cell junctions (red) or at the periphery of the cells (blue). **b,** Jurkat-CD40-GFP cells were incubated with ChiLob 7/4 m1 affinity mutants as indicated for 3 hours at 37ºC and then imaged by confocal. Green: CD40-GFP. Scale bar: 4 μm. Image representative of at least fifteen images taken from 3 independent experiments. **c,** Same experiment as (**b**) Left panel: cell circularity was measured by ImageJ for five confocal images per treatment and the results of three independent experiments were pooled. Each dot represents one cell. Right panel: plot showing cumulative circularity data as a function of B cell proliferation. Means ± SEM. **d,** Binding of Fab fragments of ChiLob 7/4 m1 affinity mutants to Ramos cells. Data representative of 3 independent experiments. **e,** Jurkat-NFκB-GFP-CD40 reporter cells were incubated with various ChiLob 7/4 m1 affinity mutant IgG versus Fab pairs for 6 hours and the level of NFκB activation (GFP) assessed. Means ± SEM, n = 3, data representative of 3 independent experiments. **f**, Same experiment as (**b**) evaluating the clustering potential of 4 different ChiLob 7/4 m1affinity mutant Fab versus an IgG positive control. Clustering index calculated as indicated in (**a**). Means ± SEM, n = 5, data representative of 3 independent experiments. **g,** Ramos cells were treated with AF488-labelled ChiLob 7/4 m1 affinity mutants for 10, 30, 60, 120 or 180 minutes (left to right) at 37 ºC or 4ºC as indicated. Cells were then washed and half the cells treated with anti-AF488 mAb at 4ºC to quench cell surface associated AF488 fluorescence. Remaining cell surface-bound CD40 was expressed as % Total expression. Data representative of 3 independent experiments. **h,** Jurkat-CD40-GFP cells were incubated with ChiLob 7/4 m1 affinity mutants as indicated for 3 hours at 37ºC and then fixed with PFA, counterstained with DAPI and imaged by confocal. Orthogonal images shown. Blue: nucleus; Green: CD40-GFP. Image representative of at least ten images taken from 3 independent experiments.

Extended Data Figure 8. Super-resolution dSTORM analysis of receptor clusters induced by low affinity anti-CD40 mAb or CD40L. a, Jurkat-CD40-GFP cells were incubated with various CD40 agonists as indicated for 1 hour, and then CD40-GFP detected with AF647-conjugated anti-GFP nanobody and visualised by wide field fluorescence microscopy and dSTORM. A region of interest was drawn around the cell:cell junctions and clustering analysis was performed using HDBSCAN, example results of subclusters are shown. Scale bars; 10 μm (wide field), 5 μm (dSTORM), 1 μm (HDBSCAN) **b,** Subcluster density (number of localisation per unit area). One-way ANOVA followed by Kruskal-Wallis test, *p < 0.05, **p < 0.01, ***p < 0.001, ****p < 0.0001. n= number of subclusters, y=number of cell:cell junctions examined: Untreated, n=281, y=28; ChiLob 7/4 h2, n=664, y=26; CD40L, n=427, y=25; WT m1, n=138, y=23; FW-16 m1, n=642, y=29; FW-32 m1, n=151, y=30. **c,** Plot of subcluster area versus density. Results shown are representative of 3 independent experiments.

Extended Data Figure 9. Characterization of low affinity utomilumab and nivolumab variants. a, Utomilumab affinity mutants were evaluated for their binding affinity for 4-1BBECD by SPR, with affinity constants (ka, kd and KD) calculated as well as fold change which indicates affinity change compared with WT utomilumab. **b,** Jurkat-4-1BB-GFP cells were incubated with utomilumab affinity mutants and then imaged by confocal. Green: 4-1BB-GFP. Scale bar: 4 μm. Images representative of at least fifteen images taken from 3 independent experiments. **c,** Same experiment as (**b**) Left panel: cell circularity was measured by ImageJ for five confocal images per treatment and the results of three independent experiments were pooled. Each dot represents one cell. Right panel: plot showing cumulative circularity data as a function of NFκB activation. Means ± SEM. **d,** The expression level of 4-1BB on Ramos-4-1BB cells was analysed by flow cytometry. **e,** The expression level of 4-1BB on IIA1.6-4-1BB cells was analysed by flow cytometry. **f,** SPR of various nivolumab affinity mutants injected at 250, 50, 10, 2, 0.4, and 0 nM binding to PD-1ECD. Plots display sensorgram data representative of 3 independent experiments. **g,** Nivolumab affinity mutants were evaluated for their binding affinity for PD-1ECD by SPR as indicated in **f**, with affinity constants (ka, kd and KD)

calculated. Fold change indicates affinity change compared with WT nivolumab. **h,** PD-1-transfected Jurkat cells were incubated with various nivolumab affinity mutants as indicated and then washed and bound hIgG detected. Means ± SEM, n = 3, data representative of 3 independent experiments.

Extended Data Figure 10. Low affinity nivolumab variants induce PD-1 agonism through receptor clustering. a, Schematic of assays investigating the antagonistic and agonistic properties of anti-PD-1 affinity mutants. Left panel: Assay to evaluate the ability of mAb to block PD-L1-mediated T cell suppression. Middle panel: Assay to evaluate the ability of mAb to induce PD-1 signalling. Right panel: Assay to evaluate the ability of mAb to suppress anti-CD3 mAb-mediated T cell activation. **b,** Histogram showing CHO-SB2H2-scFv-CD8α cells binding to various nivolumab affinity mutants, data representative of 3 independent experiments. **c,** CHO-SB2H2-scFv-CD8α cells were opsonized with OKT3 and nivolumab affinity mutants as indicated and then co-cultured with Jurkat-NFAT-Luc-PD-1 for 6 hours. NFAT signalling activity was then assessed. Plots showing relative luciferase units (RLU) vs ka and RLU vs kd. Means ± SEM, n = 3, data representative of 3 independent experiments. **d,** Same experiment as (**c**). Plots showing CD69 MFI vs ka and RLU vs CD69 MFI. **e,** IIA1.6-PD-1-GFP cells were incubated with nivolumab affinity mutants for 3 hours and then imaged using confocal. Green: PD-1-GFP. Scale bar: 4 μm. Image representative of at least 15 images taken from 3 independent experiments. **f,** IIA1.6-PD-1-GFP cells were incubated with nivolumab affinity mutants as indicated for 3 hours and then fixed, counterstained with DAPI and imaged using confocal. Z-stack projections shown. Blue: nucleus; Green: PD-1-GFP. Scale bar: 4 μm. Image representative of at least ten images taken from two independent experiments. **g,** Jurkat-NFκB-GFP-PD-1 reporter cells were incubated with various nivolumab affinity mutants as indicated for 30 minutes then, Left panel: washed with the level of mAb remaining bound after various periods quantified or Right panel: the level of NFκB activation (GFP) assessed after various periods. Means ± SEM, n = 3, data representative of 3 independent experiments. **h,** Same experiment as (**e**) Left panel: cell circularity was measured by ImageJ for five confocal images per treatment and the results of three independent experiments were pooled. Each dot

represents one cell. Right panel: plot showing cumulative circularity data as a function of CD69 MFI, Means ± SEM, n = 34, 32, 39, 39, 36, 38, 33, 36, 33, 37 (from left to right).

Extended Data Figure 11. Low affinity mutants retain target-specific binding and exhibit agonism at multiple receptor densities. a, Heat map showing MFI values of ChiLob 7/4 m1 affinity mutants binding to Jurkat-NFκB-GFP-TNFRII cells versus a positive control anti-TNFRII mAb. **b,** Heat map showing SPR response of ChiLob 7/4 m1 affinity mutants binding to soluble TNFRII immobilized onto a CM5 chip versus a positive control anti-TNFRII mAb. **c,** Heat map showing MFI values of utomilumab affinity mutants binding to Jurkat-NFκB-GFP-CD27 cells versus a positive control anti-CD27 mAb. **d,** Heat map showing SPR response of utomilumab affinity mutants binding to soluble CD27 immobilized onto a CM5 chip versus a positive control anti-CD27 mAb. **e,** Heat map showing MFI values of nivolumab affinity mutants binding to Jurkat-CD28-GFP cells versus a positive control anti-CD28 mAb. **f,** Heat map showing SPR response of nivolumab affinity mutants binding to soluble CD28 immobilized onto a CM5 chip versus a positive control anti-CD28 mAb. **g,** Representative z plane images covering the entire z-axis of Jurkat-CD40-GFP cells treated with anti-CD40 mAb. Blue: nucleus; Green: PD-1-GFP. Scale bar: 4 μm. Data representative of 3 independent experiments. **h,** Representative z plane images covering the entire z-axis of Jurkat-4-1BB-GFP cells treated with anti-4-1BB mAb. Blue: nucleus; Green: PD-1-GFP. Scale bar: 4 μm. Data representative of 3 independent experiments. **i,** Representative z plane images covering the entire z-axis of IIA1.6-PD-1-GFP cells treated with anti-PD-1 mAb. Blue: nucleus; Green: PD-1-GFP. Scale bar: 4 μm. Data representative of 3 independent experiments. **j,** Jurkat-NFκB-GFP reporter cells expressing low, medium or high levels of CD40 were incubated with various ChiLob 7/4 m1 affinity mutants for 6 hours and the level of NFκB activation (GFP) assessed. **k,** Quantification of CD40 receptor number (as expressed by Molecules of Equivalent Soluble Fluorochrome, MESF) on various cell lines and primary cells as indicated. **l,** Jurkat-NFκB-GFP reporter cells expressing low, medium or high levels of PD-1 were incubated with various nivolumab affinity mutants for 6 hours and the level of NFκB activation (GFP) assessed. **m,** Quantification of PD-1 receptor number (MESF) on various cell lines and primary cells as indicated. **n,**

Jurkat-NFκB-GFP reporter cells expressing low, medium or high levels of 4-1BB were incubated with various utomilumab affinity mutants for 6 hours and the level of NFκB activation (GFP) assessed. **o,** Quantification of 4-1BB receptor number (MESF) on various cell lines and primary cells as indicated. **p,** mAb (black) or soluble ligands (red) were injected at 250, 50, 10, 2, 0.4, and 0 nM to evaluate binding by SPR to their cognate soluble receptor CD40, 4-1BB or PD-1, as indicated. Values indicate the equilibrium affinity KD of the ligands for their cognate receptor. Means ± SEM, n = 3, data representative of 3 independent experiments.

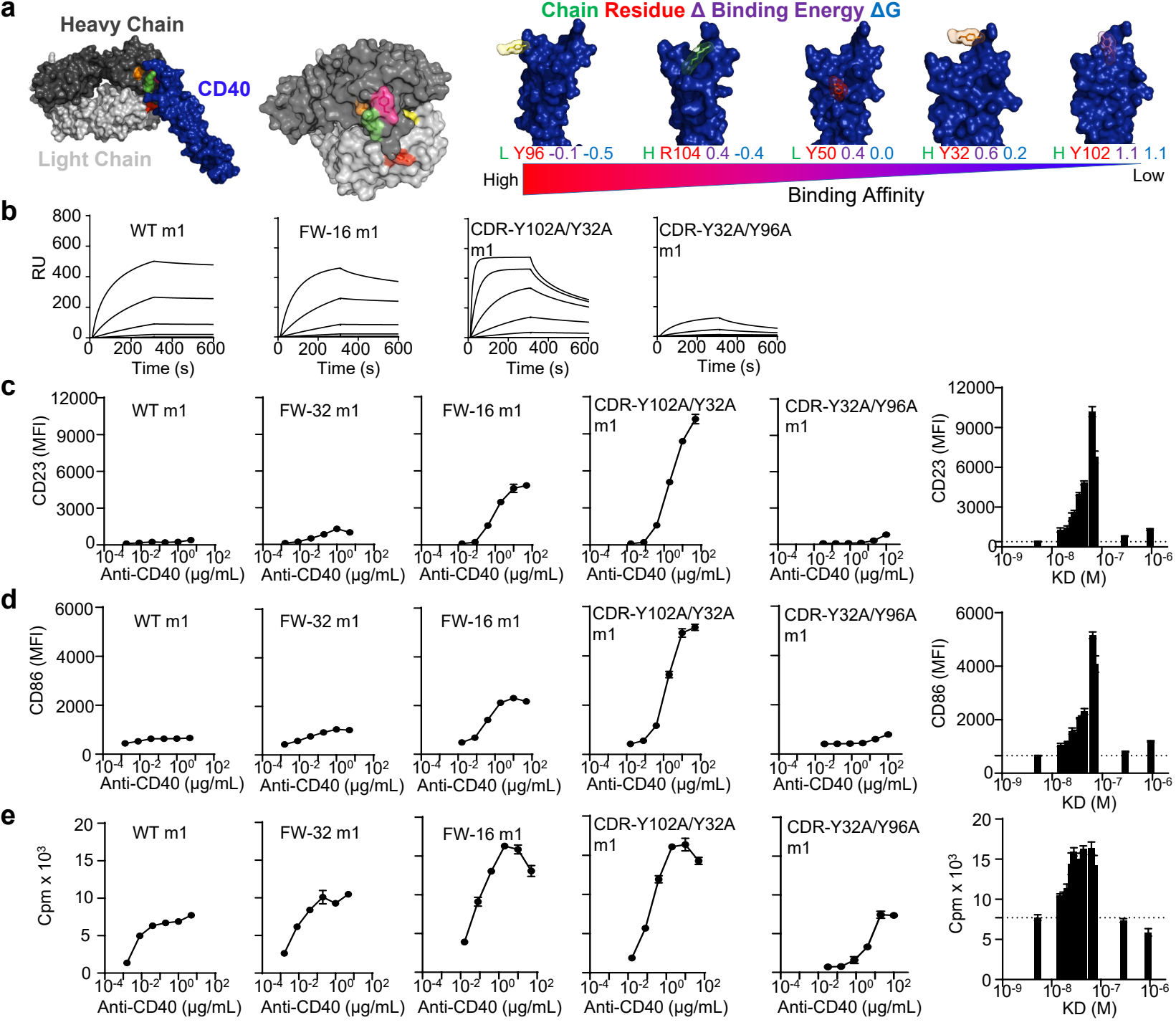
a
Heavy Chain
CD40
Light Chain
Chain Residue Δ Binding Energy ΔG
L Y96 -0.1 -0.5
H R104 0.4 -0.4
L Y50 0.4 0.0
H Y32 0.6 0.2
H Y102 1.1 1.1
High
Low
Binding Affinity
b
RU
WT m1
FW-16 m1
CDR-Y102A/Y32A m1
CDR-Y32A/Y96A m1
Time (s)
c
CD23 (MFI)
WT m1
FW-32 m1
FW-16 m1
CDR-Y102A/Y32A m1
CDR-Y32A/Y96A m1
Anti-CD40 (μg/mL)
KD (M)
d
CD86 (MFI)
e
Cpm x 10³

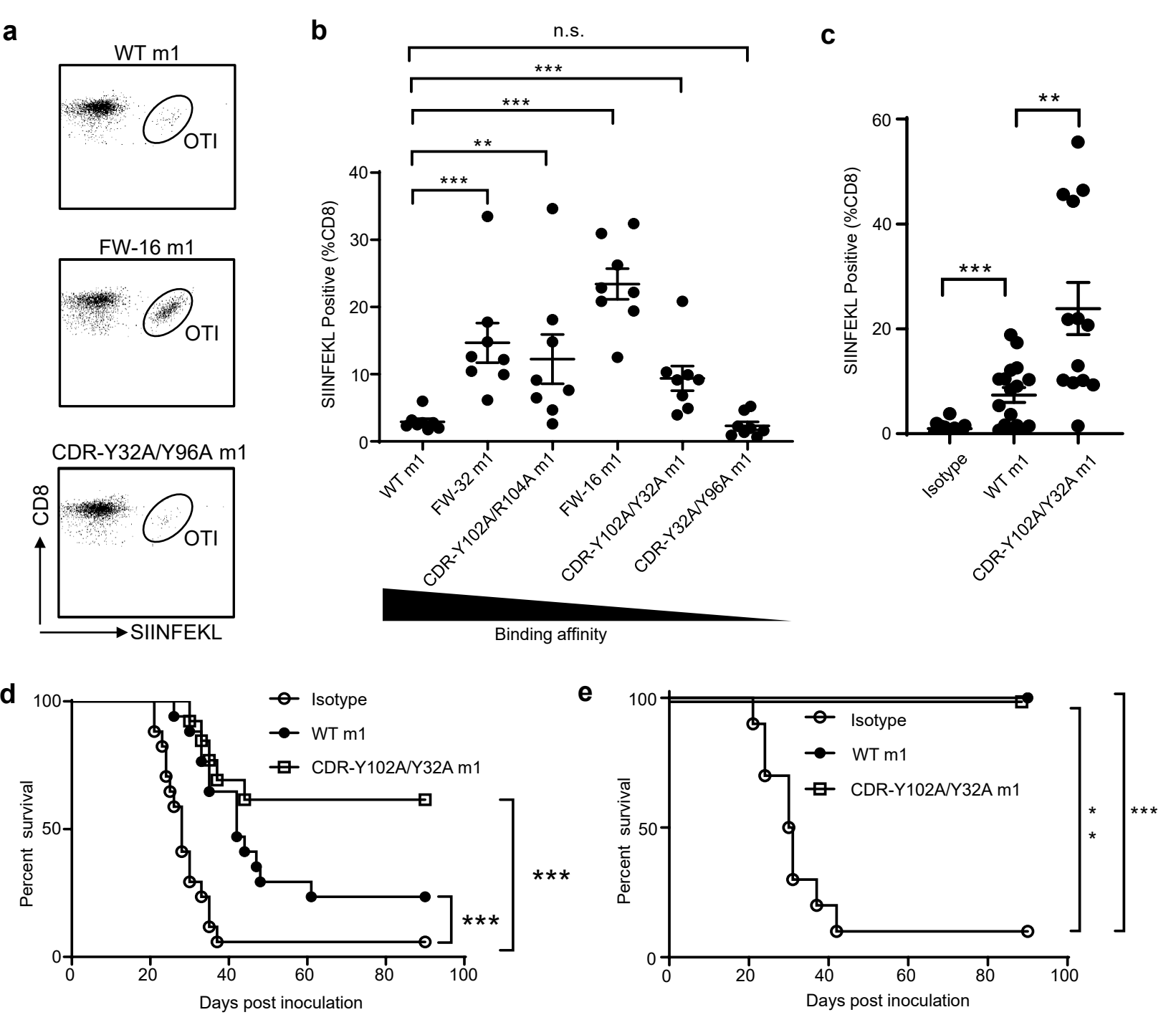
a
WT m1
OTI
FW-16 m1
OTI
CDR-Y32A/Y96A m1
OTI
CD8
SIINFEKL
b
n.s.
***
***
**
***
SIINFEKL Positive (%CD8)
0
10
20
30
40
WT m1
FW-32 m1
CDR-Y102A/R104A m1
FW-16 m1
CDR-Y102A/Y32A m1
CDR-Y32A/Y96A m1
Binding affinity
c
**
***
SIINFEKL Positive (%CD8)
0
20
40
60
Isotype
WT m1
CDR-Y102A/Y32A m1
d
Isotype
WT m1
CDR-Y102A/Y32A m1
Percent survival
0
50
100
0
20
40
60
80
100
Days post inoculation
***
***
e
Isotype
WT m1
CDR-Y102A/Y32A m1
Percent survival
0
50
100
0
20
40
60
80
100
Days post inoculation
**
***

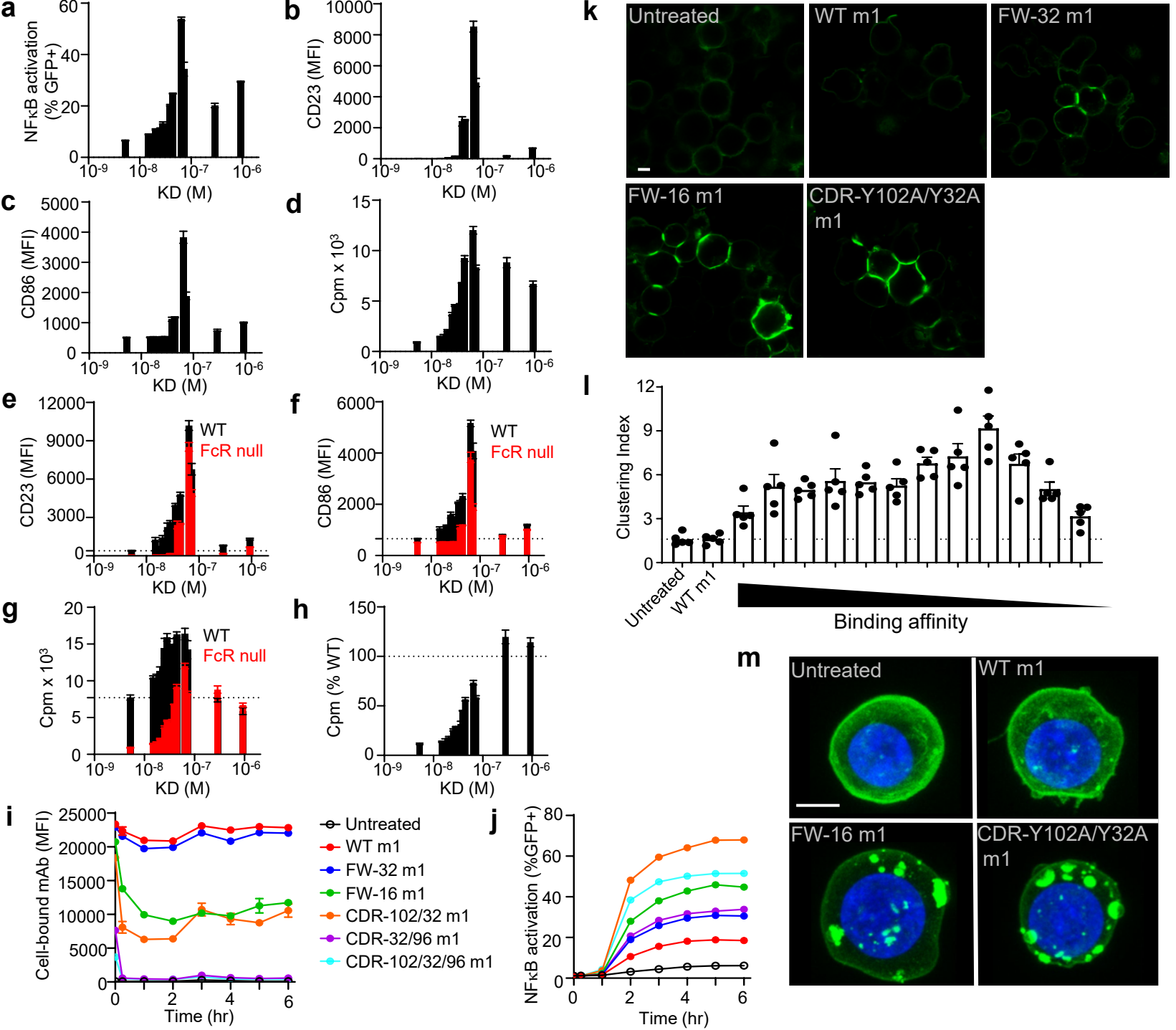
a
NFκB activation (% GFP+)
KD (M)
b
CD23 (MFI)
KD (M)
c
CD86 (MFI)
KD (M)
d
Cpm x 10³
KD (M)
e
CD23 (MFI)
WT
FcR null
KD (M)
f
CD86 (MFI)
WT
FcR null
KD (M)
g
Cpm x 10³
WT
FcR null
KD (M)
h
Cpm (% WT)
KD (M)
k
Untreated
WT m1
FW-32 m1
FW-16 m1
CDR-Y102A/Y32A m1
l
Clustering Index
Untreated
WT m1
Binding affinity
m
Untreated
WT m1
FW-16 m1
CDR-Y102A/Y32A m1
i
Cell-bound mAb (MFI)
Time (hr)
Untreated
WT m1
FW-32 m1
FW-16 m1
CDR-102/32 m1
CDR-32/96 m1
CDR-102/32/96 m1
j
NFκB activation (%GFP+)
Time (hr)

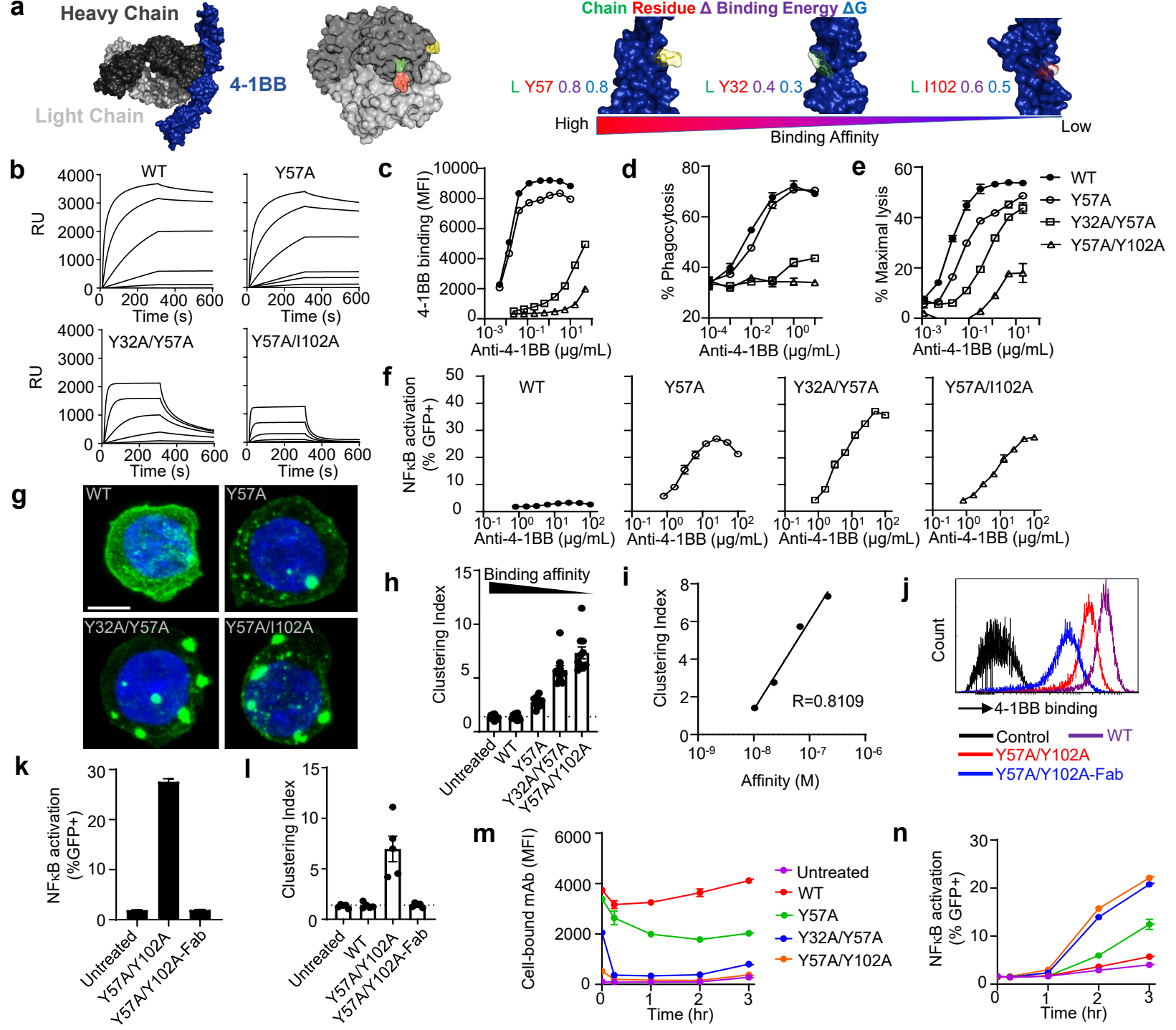
a
Heavy Chain
Light Chain
4-1BB
Chain Residue Δ Binding Energy ΔG
L Y57 0.8 0.8
L Y32 0.4 0.3
L I102 0.6 0.5
High
Low
Binding Affinity
b
WT
Y57A
Y32A/Y57A
Y57A/I102A
RU
Time (s)
c
4-1BB binding (MFI)
Anti-4-1BB (μg/mL)
d
% Phagocytosis
Anti-4-1BB (μg/mL)
e
% Maximal lysis
Anti-4-1BB (μg/mL)
WT
Y57A
Y32A/Y57A
Y57A/Y102A
f
NFκB activation (% GFP+)
Anti-4-1BB (μg/mL)
g
WT
Y57A
Y32A/Y57A
Y57A/I102A
h
Binding affinity
Clustering Index
Untreated
WT
Y57A
Y32A/Y57A
Y57A/Y102A
i
Clustering Index
R=0.8109
Affinity (M)
j
Count
4-1BB binding
Control
WT
Y57A/Y102A
Y57A/Y102A-Fab
k
NFκB activation (%GFP+)
Untreated
Y57A/Y102A
Y57A/Y102A-Fab
l
Clustering Index
Untreated
WT
Y57A/Y102A
Y57A/Y102A-Fab
m
Cell-bound mAb (MFI)
Time (hr)
Untreated
WT
Y57A
Y32A/Y57A
Y57A/Y102A
n
NFκB activation (% GFP+)
Time (hr)

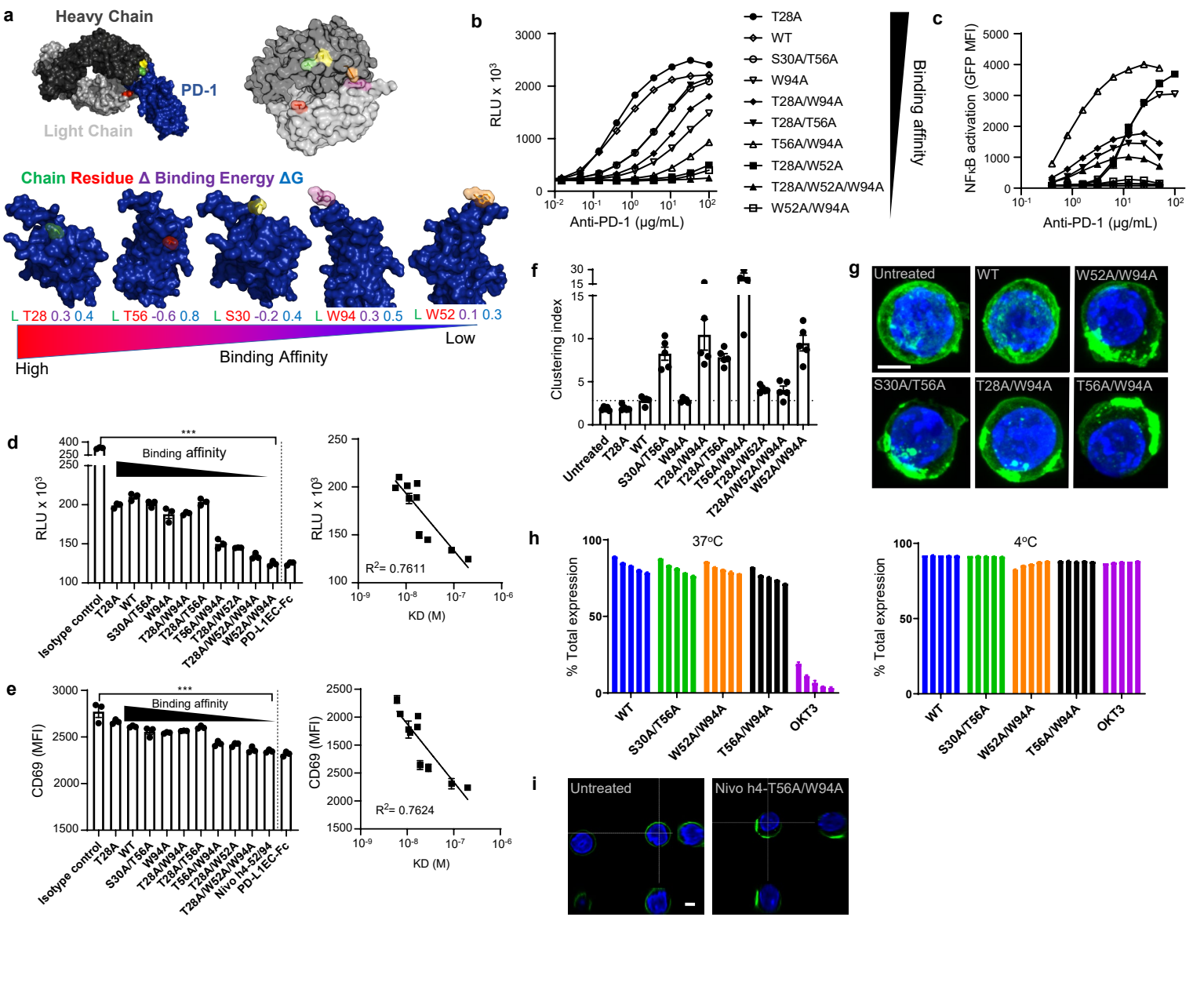
a
Heavy Chain
PD-1
Light Chain
Chain Residue Δ Binding Energy ΔG
L T28 0.3 0.4
L T56 -0.6 0.8
L S30 -0.2 0.4
L W94 0.3 0.5
L W52 0.1 0.3
High
Binding Affinity
Low
b
RLU x 10^3
Anti-PD-1 (μg/mL)
T28A
WT
S30A/T56A
W94A
T28A/W94A
T28A/T56A
T56A/W94A
T28A/W52A
T28A/W52A/W94A
W52A/W94A
Binding affinity
c
NFκB activation (GFP MFI)
Anti-PD-1 (μg/mL)
d
Binding affinity
RLU x 10^3
Isotype control
T28A
WT
S30A/T56A
W94A
T28A/W94A
T28A/T56A
T56A/W94A
T28A/W52A
T28A/W52A/W94A
W52A/W94A
PD-L1EC-Fc
R2= 0.7611
KD (M)
e
Binding affinity
CD69 (MFI)
Isotype control
T28A
WT
S30A/T56A
W94A
T28A/W94A
T28A/T56A
T56A/W94A
T28A/W52A
T28A/W52A/W94A
Nivo h4-52/94
PD-L1EC-Fc
R2= 0.7624
KD (M)
f
Clustering index
Untreated
T28A
WT
S30A/T56A
W94A
T28A/W94A
T28A/T56A
T56A/W94A
T28A/W52A
T28A/W52A/W94A
W52A/W94A
g
Untreated
WT
W52A/W94A
S30A/T56A
T28A/W94A
T56A/W94A
h
37°C
4°C
% Total expression
WT
S30A/T56A
W52A/W94A
T56A/W94A
OKT3
i
Untreated
Nivo h4-T56A/W94A